

A Cosmological Fireball with Thirty-Percent Gamma-Ray Radiative Efficiency

Liang Li (✉ liliang135136@163.com)

ICRANet

Yu Wang

Sapienza University of Rome

Felix Ryde

KTH Royal Institute of Technology

Asaf Pe'er

Bar-Ilan University

Bing Zhang

University of Nevada, Las Vegas <https://orcid.org/0000-0002-9725-2524>

Sylvain Guiriec

The George Washington University

Alberto Castro-Tirado

IAA-CSIC

David Alexander Kann

Instituto de Astrofísica de Andalucía <https://orcid.org/0000-0003-2902-3583>

Magnus Axelsson

Royal Institute of Technology (KTH)

Kim Page

University of Leicester <https://orcid.org/0000-0001-5624-2613>

Peter Veres

University of Alabama Huntsville

Narayana Perumpalli Bhat

University of Alabama Huntsville

Letter

Keywords: gamma-ray bursts (GRBs), radiative efficiency

Posted Date: February 17th, 2021

DOI: <https://doi.org/10.21203/rs.3.rs-231408/v1>

License: © ⓘ This work is licensed under a Creative Commons Attribution 4.0 International License.

[Read Full License](#)

A Cosmological Fireball with Thirty-Percent Gamma-Ray Radiative Efficiency

Liang Li^{1,2,3*}, Yu Wang^{1,2,3*}, Felix Ryde⁴, Asaf Pe'er⁵, Bing Zhang^{6*}, Sylvain Guiriec^{7,8}, Alberto J. Castro-Tirado^{9,10}, D. Alexander Kann⁹, Magnus Axelsson¹¹, Kim Page¹², Péter Veres¹³, P. N. Bhat^{13,14}

¹*ICRANet, Piazza della Repubblica 10, 65122 Pescara, Italy*

²*INAF – Osservatorio Astronomico d’Abruzzo, Via M. Maggini snc, I-64100, Teramo, Italy*

³*Dip. di Fisica and ICRA, Sapienza Università di Roma, Piazzale Aldo Moro 5, I-00185 Rome, Italy*

⁴*Department of Physics, KTH Royal Institute of Technology, and the Oskar Klein Centre for Cosmoparticle Physics, 10691 Stockholm, Sweden*

⁵*Department of Physics, Bar-Ilan University, Ramat-Gan 52900, Israel*

⁶*Department of Physics and Astronomy, University of Nevada, Las Vegas, NV 89154, USA*

⁷*Department of Physics, The George Washington University, 725 21st Street NW, Washington, DC 20052, USA*

⁸*NASA Goddard Space Flight Center, Greenbelt, MD 20771, USA*

⁹*Instituto de Astrofísica de Andalucía (IAA-CSIC), PO Box 03004, Granada, Spain*

¹⁰*Departamento de Ingeniería de Sistemas y Automática, Escuela de Ingenierías, Universidad de Málaga, Málaga, Spain*

¹¹*Department of Astronomy, Stockholm University, SE-106 91 Stockholm, Sweden*

¹²*School of Physics and Astronomy, University of Leicester, University Road, Leicester LE1 7RH, UK*

¹³*Center for Space Plasma and Aeronomic Research, University of Alabama in Huntsville, Huntsville, AL, USA*

¹⁴*Space Science Department, University of Alabama in Huntsville, Huntsville, AL, USA*

*E-mail: liang.li@icranet.org; yu.wang@uniroma1.it; zhang@physics.unlv.edu

Gamma-ray bursts (GRBs) are the most powerful explosions in the universe. The composition of the jets is, however, subject to debate^{1,2}. Whereas the traditional model invokes a relativistic matter-dominated fireball with a bright photosphere emission component³, the lack of the detection of such a component in some GRBs⁴ has led to the conclusion that GRB jets may be Poynting-flux-dominated⁵. Furthermore, how efficiently the jet converts its energy to radiation is poorly constrained. A definitive diagnosis of the GRB jet composition and measurement of GRB radiative efficiency requires high-quality prompt emission and afterglow data, which has not been possible with the sparse observations in the past. Here we report a comprehensive temporal and spectral analysis of the TeV-emitting bright GRB 190114C. Its fluence is one of the highest of all GRBs detected so far, which allows us to perform a high-significance study on the prompt emission spectral properties and their variations down to a very short timescale of about 0.1 s. We identify a clear thermal component during the first two prompt emission episodes, which is fully consistent with the prediction of the fireball photosphere model. The third episode of the prompt emission is consistent with synchrotron radiation from the deceleration of the fireball. This allows us to directly dis-

sect the fireball energy budget in a parameter-independent manner⁶ and robustly measure a nearly 30% radiative efficiency for this GRB. The afterglow microphysics parameters can be also well constrained from the data. GRB 190114C, therefore, exhibits the evolution of a textbook-version relativistic fireball, suggesting that fireballs can indeed power at least some GRBs with high efficiency.

On 14 January 2019 at 20:57:02.63 Universal Time (UT) (hereafter T_0), an ultra-bright burst, GRB 190114C, was first triggered on by the Gamma-ray Burst Monitor (GBM) onboard the *Fermi* Gamma-ray Space Telescope⁷ and the *Neil Gehrels Swift* Observatory's (*Swift* hereafter) Burst Alert Telescope (BAT)⁸. Soon after, the Large Area Telescope (LAT) onboard *Fermi*, *Konus-Wind*, *INTEGRAL/SPI-ACS*, *AGILE/MCAL*, and the *Insight-HXMT/HE* were also triggered. Long-lasting and multi-wavelength afterglow observations were carried out by *Swift* in the X-ray and optical bands, and by several ground-based optical and radio telescopes (such as GROND⁹, GTC¹⁰, VLA¹¹, MeerKAT¹²).

The prompt emission lightcurve (Figure 1) consists of three distinct emission episodes. The first emission episode (i.e., P_1) starts at $\sim T_0$ and lasts for ~ 2.35 s, the second emission episode (i.e., P_2) exhibits multiple peaks and lasts from $\sim T_0+2.35$ s to $\sim T_0+15$ s, and the significantly fainter third emission episode (i.e., P_3) extends from $\sim T_0+15$ s to $\sim T_0+25$ s. First, P_1 and P_2 exhibit a non-thermal and a sub-dominant thermal component as first discovered in Ref.¹³. The thermal components in P_1 and P_2 evolve independently (Figure 2). Such a feature provides a unique opportunity to study the jet composition and photosphere properties at distinctly different epochs of central engine activities. Second, the non-thermal spectral shape in P_3 is consistent with a synchrotron-radiation origin from afterglow emission^{14,15}. The afterglow phase of this GRB has the most complete observations in terms of spectral coverage, from radio all the way to TeV gamma-rays. This provides another unique opportunity to study the GRB afterglow properties within the framework of synchrotron and synchrotron self-Compton model.

We perform a time-resolved spectral analysis for the *Fermi*-GBM observations. Thanks to its high fluence of $(4.436 \pm 0.005) \times 10^{-4}$ erg cm⁻² as the fifth highest fluence GRB ever observed with *Fermi*-GBM, we were able to divide its T_{90} (measured as the time interval between when 5% and 95% of the total flux was recorded) duration (116 s) into 48 slices, with each time bin containing enough photons to conduct a high-significance spectral analysis (see Methods). The CPL+BB (CPL: Cutoff powerlaw, BB: Blackbody) model^{13,16} gives a better fit in comparison with the CPL model and other models (see Methods) from $T_0+0.55$ s to $T_0+1.93$ s in P_1 (includes 8 slices, hereafter P_1^{th}) and from $T_0+2.45$ s to $T_0+5.69$ s in P_2 (includes 16 slices, hereafter P_2^{th}) based on the deviance information criterion (DIC). P_1^{th} and P_2^{th} correspond to the peak flux of the P_1 and P_2 , respectively, which precisely correspond to the epochs when the power-law index α of the single CPL fits (see Methods) are beyond the limits of the synchrotron line of death¹⁷, i.e. $\alpha > -2/3$. This is an indication of the existence of a thermal component as also reported in Ref.¹⁶. An example of an νF_ν spectrum for one time slice (4.95 s–5.45 s) with the CPL+BB model giving the best fit is displayed in Figure 3. In this example, a thermal component is superimposed on the CPL component that is presumably of a synchrotron origin.

We compared the properties of the thermal components identified in P_1 and P_2 . The evolutions of the characteristic temperatures (kT) in P_1 and P_2 follow distinct broken power-law decays: a smooth decay of the temperature followed by a fast drop (see the left panel in Figure 2). The temporal feature in each individual pulse is consistent with the typical observations that showed a temperature evolution with a broken power law in time^{18,19}, but such a feature in two independent pulses in one burst has never been identified in previous observations. The temporal behaviours showing different decay indices between two different pulses within a single GRB suggests that the GRB central engine ejects distinct independent jet components during its active phase. We note that several GRBs with statistically significant thermal components have been observed by BATSE, Konus, *Swift*, and *Fermi* before^{13,16,20,21}. However, they are either single-pulse bursts (e.g. GRB 110721A²¹), or highly overlapping multi-pulse bursts (e.g. GRB 090902B²⁰), or their thermal emission component is not strong enough (e.g. GRB 100724B¹³), so that the photosphere properties could not be studied in detail among distinct pulses. The unique advantages of GRB 190114C, i.e. its low redshift, high fluence, several well-separated pulses in one single GRB, and a strong thermal component, make such a study possible.

Within the framework of the standard fireball photosphere model²², we can infer the photosphere characteristics and the ratio of thermal to non-thermal emission to obtain information on the jet properties, such as the bulk Lorentz factor Γ and the initial size of the jet r_0 . Figures 2 and Extended Data 2 show the evolution of the bulk Lorentz factor Γ and the parameter \mathfrak{R} (the effective transverse size of the emitting region¹⁹), respectively; they exhibit similar temporal behaviors in P_1 and P_2 , i.e., a broken power-law evolution behavior, with \mathfrak{R} increasing with time and Γ decreasing over time. The comparison of the properties with a global view is summarised in Table 1. The best-fitting results of the relevant parameters with a power-law model are listed in Table 2.

The time-resolved analysis shows that almost all the low-energy photon index α values of the CPL-only fits in P_3 are much softer than those in P_1 and P_2 (Figure 1), suggesting that the emission has a different origin. α gradually decreases toward -2 (similar to the results reported in Ref.¹⁶), a typical value for synchrotron radiation, which indicates that the fireball is entering the afterglow phase. Assuming that the peak time of P_3 is the deceleration time when the mass of the ambient medium collected by the forward shock is comparable to $1/\Gamma$ of the mass entrained in the fireball^{23,24}, one can also estimate the Lorentz factor of the fireball at the deceleration radius, Γ_0 , using an independent method (see Methods). We find that the average bulk Lorentz factors measured during the prompt emission phase ($\Gamma = 741 \pm 18$ for P_1 , $\Gamma = 571 \pm 12$ for P_2) are slightly higher than the bulk Lorentz factor measured at the deceleration radius ($\Gamma_0 = 507 \pm 5$ for P_3). This is fully consistent with the prediction of the GRB fireball model, which predicts that a fraction of the kinetic energy is dissipated during the prompt emission phase.

The derived Lorentz factors and the photosphere radii exhibit systematic variations, with the Lorentz factor decreasing from ~ 1000 to ~ 200 (Figure 2), and the photosphere radius varying on the order of 10^{12} cm (Extended Data Figure 3). This is likely related to the behavior of the GRB central engine. The decay of Γ in P_1 and P_2 is consistent with the expectation that faster ejecta from the engine tends to reach the photosphere earlier than slower ejecta, and the rapid decline at

the end of each episode may be related to the high-latitude emission of the fireball as the engine activity abruptly ceases^{25,26}. Since the Lorentz factor range is not very wide, it is expected that the deceleration of the fireball is essentially prompt without a significant energy injection phase due to the pile up of the slow materials. This is consistent with the power-law decay with time of multi-wavelength afterglow emission from the source²⁷⁻²⁹.

The above-mentioned two methods of measuring Lorentz factors both rely on some unknown parameters. By combining the photosphere data in P_1 and P_2 and the afterglow data in P_3 , one can dissect various energy components in the fireball in a parameter-independent way⁶. A systematic search for previously detected GRBs did not reveal a single case showing both a significant photosphere signature and an afterglow deceleration signature⁶. GRB 190114C therefore provides the first case with which a parameter-independent diagnosis of fireball parameters can be carried out. We perform a time-integrated spectral fit to the prompt emission spectrum of P_1 and P_2 (0.55 - 1.93 s and 2.45-5.69 s) with the CPL+BB model and derived the observed properties (including both the thermal and non-thermal components) of the fireball as shown in Table 3. Following Ref.⁶ (Methods), we can for the first time robustly derive the following physical parameters of a GRB fireball (Table 3): initial dimensionless specific enthalpy density $\eta = 708 \pm 8$, bulk Lorentz factor at the photosphere $\Gamma_{\text{ph}} = 666 \pm 6$, bulk Lorentz factor before deceleration $\Gamma_0 = 507 \pm 5$, and fireball isotropic-equivalent mass loading $M_{\text{iso}} = (8.6 \pm 0.6) \times 10^{-4} M_{\odot}$. This gives a direct measurement of the fireball radiative efficiency $\eta_{\gamma} = (28.3 \pm 1.4)\%$. This measured efficiency has much smaller uncertainties than the values derived for previous GRBs using afterglow modeling^{30,31}. A high fireball radiative efficiency has been theorized in the past but with a large uncertainty^{3,32}. Our measured $\eta_{\gamma} \sim 30\%$ suggests that a GRB fireball can indeed emit both thermal and non-thermal gamma-rays efficiently.

With the solved fireball parameters, the isotropic kinetic energy of the fireball at the afterglow phase is measured as $E_{\text{k,iso}} \simeq 7.8 \times 10^{53}$ erg. This allows us to make use of this prompt-emission-measured $E_{\text{k,iso}}$ in the afterglow model to constrain shock microphysics parameters (Methods). Using broad-band afterglow data, we can derive an electron injection power law index $p \simeq 2.85$ and the inverse Compton parameter $Y \sim 0.75$. This leads to the solution to the two equipartition parameters of electrons and magnetic fields: $\epsilon_e \simeq 0.14$ and $\epsilon_B \sim 9 \times 10^{-4}$ (Methods). These parameters are usually poorly constraints in other GRBs and are often assumed to perform modeling. We are able to measure these values precisely, which are also broadly consistent with the more detailed afterglow modeling on the event²⁹.

References

1. Pe'er, A. Physics of Gamma-Ray Bursts Prompt Emission. *Advances in Astronomy* **2015**, 907321 (2015). 1504.02626.
2. Zhang, B. *The Physics of Gamma-Ray Bursts* (2018).
3. Mészáros, P. & Rees, M. J. Steep Slopes and Preferred Breaks in Gamma-Ray Burst Spectra: The Role of Photospheres and Comptonization. *The Astrophysical Journal* **530**, 292–298 (2000). astro-ph/9908126.
4. Abdo, A. A. *et al.* Fermi Observations of GRB 090902B: A Distinct Spectral Component in the Prompt and Delayed Emission. *The Astrophysical Journal Letters* **706**, L138–L144 (2009). 0909.2470.
5. Zhang, B. & Pe'er, A. Evidence of an Initially Magnetically Dominated Outflow in GRB 080916C. *The Astrophysical Journal Letters* **700**, L65–L68 (2009). 0904.2943.
6. Zhang, B., Wang, Y. & Li, L. Dissecting Energy Budget of a Gamma-Ray Burst Fireball. *arXiv e-prints* arXiv:2102.04968 (2021). 2102.04968.
7. Hamburg, R. *et al.* GRB 190114C: Fermi GBM detection. *GRB Coordinates Network, Circular Service, No. 23707, #1* (2019) **23707** (2019).
8. J.D. Gropp *et al.* GRB 190114C: Swift detection of a very bright burst with a bright optical counterpart. *GRB Coordinates Network* (2019).
9. Bolmer, J. & Schady, P. GRB 190114C: GROND detection of the afterglow. *GRB Coordinates Network* **23702**, 1 (2019).
10. Castro-Tirado, A. J. *et al.* GRB 190114C: refined redshift by the 10.4m GTC. *GRB Coordinates Network* **23708**, 1 (2019).
11. Alexander, K. D., Laskar, T., Berger, E., Mundell, C. G. & Margutti, R. GRB 190114C: VLA Detection. *GRB Coordinates Network* **23726**, 1 (2019).
12. Tremou, L. *et al.* GRB 190114C: MeerKAT radio observation. *GRB Coordinates Network* **23760**, 1 (2019).
13. Guiriec, S. *et al.* Detection of a Thermal Spectral Component in the Prompt Emission of GRB 100724B. *The Astrophysical Journal Letters* **727**, L33 (2011). 1010.4601.
14. Ajello, M. *et al.* Fermi and Swift Observations of GRB 190114C: Tracing the Evolution of High-energy Emission from Prompt to Afterglow. *The Astrophysical Journal* **890**, 9 (2020). 1909.10605.
15. Ursi, A. *et al.* AGILE and Konus-Wind Observations of GRB 190114C: The Remarkable Prompt and Early Afterglow Phases. **904**, 133 (2020).

16. Guiriec, S. *et al.* Evidence for a Photospheric Component in the Prompt Emission of the Short GRB 120323A and Its Effects on the GRB Hardness-Luminosity Relation. *The Astrophysical Journal* **770**, 32 (2013). 1210.7252.
17. Preece, R. D. *et al.* The Synchrotron Shock Model Confronts a “Line of Death” in the BATSE Gamma-Ray Burst Data. *The Astrophysical Journal Letters* **506**, L23–L26 (1998). astro-ph/9808184.
18. Ryde, F. The Cooling Behavior of Thermal Pulses in Gamma-Ray Bursts. *The Astrophysical Journal* **614**, 827–846 (2004). astro-ph/0406674.
19. Ryde, F. & Pe’er, A. Quasi-blackbody Component and Radiative Efficiency of the Prompt Emission of Gamma-ray Bursts. *The Astrophysical Journal* **702**, 1211–1229 (2009). 0811.4135.
20. Ryde, F. *et al.* Identification and Properties of the Photospheric Emission in GRB090902B. *The Astrophysical Journal Letters* **709**, L172–L177 (2010). 0911.2025.
21. Axelsson, M. *et al.* GRB110721A: An Extreme Peak Energy and Signatures of the Photosphere. *The Astrophysical Journal Letters* **757**, L31 (2012). 1207.6109.
22. Pe’er, A., Ryde, F., Wijers, R. A. M. J., Mészáros, P. & Rees, M. J. A New Method of Determining the Initial Size and Lorentz Factor of Gamma-Ray Burst Fireballs Using a Thermal Emission Component. *The Astrophysical Journal Letters* **664**, L1–L4 (2007). astro-ph/0703734.
23. Meszaros, P. & Rees, M. J. Gamma-Ray Bursts: Multiwaveband Spectral Predictions for Blast Wave Models. *The Astrophysical Journal Letters* **418**, L59 (1993). astro-ph/9309011.
24. Sari, R. & Piran, T. Predictions for the Very Early Afterglow and the Optical Flash. **520**, 641–649 (1999). astro-ph/9901338.
25. Pe’er, A. & Ryde, F. A Theory of Multicolor Blackbody Emission from Relativistically Expanding Plasmas. *The Astrophysical Journal* **732**, 49 (2011). 1008.4590.
26. Deng, W. & Zhang, B. Low Energy Spectral Index and E_p Evolution of Quasi-thermal Photosphere Emission of Gamma-Ray Bursts. *The Astrophysical Journal* **785**, 112 (2014). 1402.5364.
27. MAGIC Collaboration *et al.* Teraelectronvolt emission from the γ -ray burst GRB 190114C. **575**, 455–458 (2019).
28. Wang, Y., Li, L., Moradi, R. & Ruffini, R. GRB 190114C: An Upgraded Legend. *arXiv e-prints* (2019). 1901.07505.
29. Wang, X.-Y., Liu, R.-Y., Zhang, H.-M., Xi, S.-Q. & Zhang, B. Synchrotron Self-Compton Emission from External Shocks as the Origin of the Sub-TeV Emission in GRB 180720B and GRB 190114C. *The Astrophysical Journal* **884**, 117 (2019). 1905.11312.

30. Zhang, B. *et al.* GRB Radiative Efficiencies Derived from the Swift Data: GRBs versus XRFs, Long versus Short. *The Astrophysical Journal* **655**, 989–1001 (2007). astro-ph/0610177.
31. Beniamini, P., Nava, L., Duran, R. B. & Piran, T. Energies of GRB blast waves and prompt efficiencies as implied by modelling of X-ray and GeV afterglows. **454**, 1073–1085 (2015). 1504.04833.
32. Kobayashi, S. & Sari, R. Ultraefficient Internal Shocks. **551**, 934–939 (2001). astro-ph/0101006.

Acknowledgements

LL thanks Damien Bégué, Jochen Greiner, Hüsne Dereli-Bégué, Zeynep Acuner, Shabnam Iyyani, Yifu Cai, Yefei Yuan, Xue-Feng Wu, Michael S. Briggs, Zi-Gao Dai, and Remo Ruffini for helpful discussions. AJC-T acknowledges financial support from the State Agency for Research of the Spanish MCIU through the "Center of Excellence Severo Ochoa" award to the Instituto de Astrofísica de Andalucía (SEV-2017-0709).

Author contributions

LL led the data analysis (the spectral fittings, the tables, and the plots), and contributed to part of the physical explanations of this particular event. YW assisted the data analysis and inspired the discovery of dual thermal evaluations, and contributed to the theoretical explanation. BZ was in charge of the framework of this article, and proposed the method of deriving fireball parameters from data. FR and AP participated in the physical explanations. DAK analysed and constructed the optical lightcurve. KP analysed the *Swift*-XRT data. FR, SG and AJC-T helped with the data analysis. LL, YW, BZ, DAK and KP wrote the article. All co-authors contributed to the article.

Correspondence and requests for materials should be addressed to LL (liang.li@icranet.org), YW (yu.wang@uniroma1.it), and BZ (zhang@physics.unlv.edu).

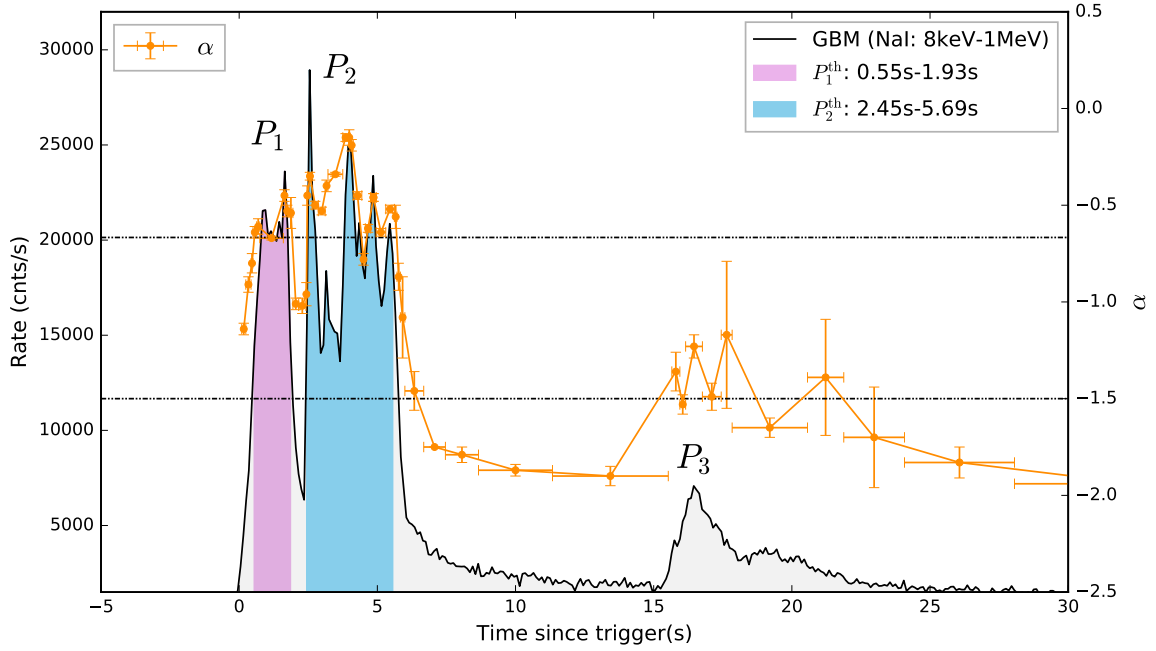


Figure 1: Count lightcurve of *Fermi*-GBM during the time span of 0 – 30 s. Two shaded regions marked with different colors denote the two independent thermally-subdominated episodes: P_1^{th} (pink) and P_2^{th} (blue). Two horizontal dashed lines represent the limiting values of $\alpha = -2/3$ and $\alpha = -3/2$ for electrons in the synchrotron slow- and fast-cooling regimes, respectively. The data points connected by solid lines (orange) represent the temporal evolution of the low-energy photon index α of the CPL-only model.

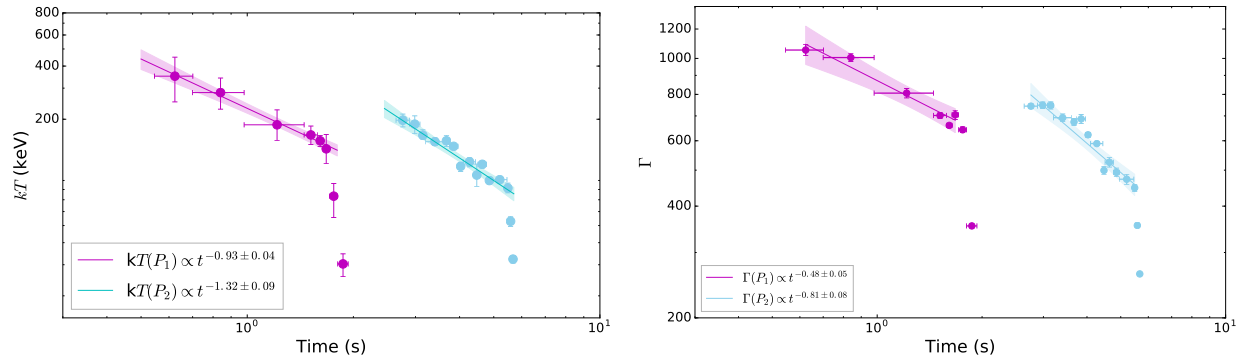


Figure 2: Temporal evolution of the temperature kT (left panel), and bulk Lorentz factor Γ (right panel). The data points indicated by pink and blue colors represent the two different pulses. Solid lines are the best power-law fits to the data for P_1 and P_1 excluding several points during the drop, and shaded areas are their 2- σ (95% confidence interval) regions. The derived time-resolved evolution of Γ is based on the photosphere properties under the framework of the traditional method²².

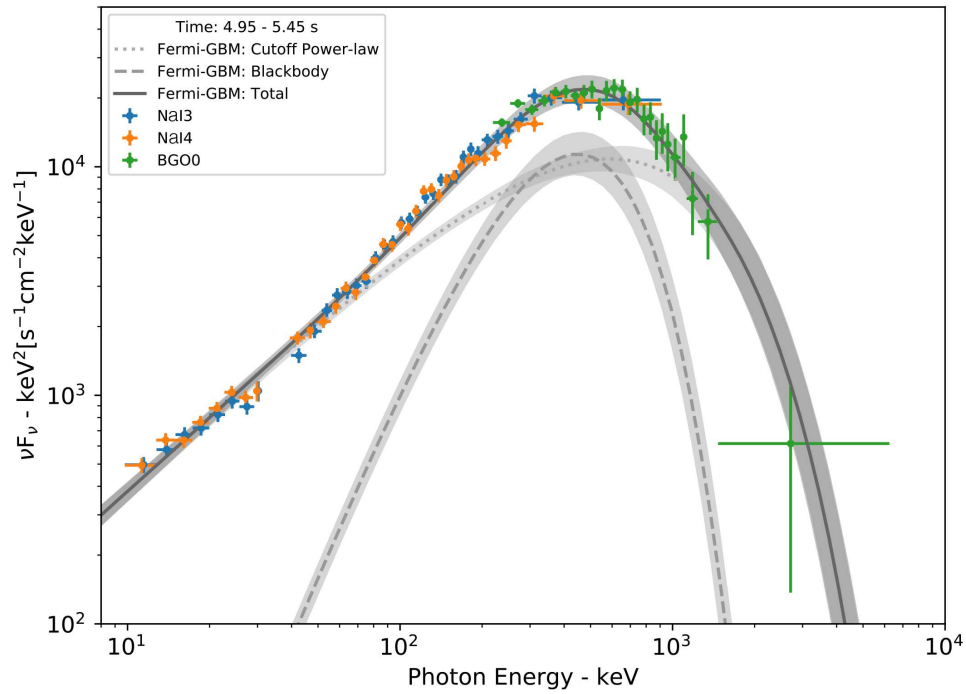


Figure 3: Spectrum from 4.95 s to 5.45 s. The spectrum includes data from *Fermi*-GBM (2 NaI and 1 BGO detector). The fitting is presented by a solid line, including the components of a Plank blackbody function by a dashed line and a cutoff power-law by a dotted line.

	GRB 190114C- P_1^{th} (From $t_{\text{obs}} = 0.55$ s to 1.93 s)	GRB 190114C- P_2^{th} (From $t_{\text{obs}} = 2.45$ s to 5.69 s)
Observed properties		
Duration (s)	1.38 s	3.24 s
E_c (keV)	$337.4^{+26.9}_{-27.2}$	$604.8^{+16.8}_{-16.5}$
kT (keV)	$267.0^{+22.2}_{-18.2}$	$144.7^{+3.4}_{-3.4}$
F_{BB} (erg cm $^{-2}$ s $^{-1}$)	$(1.51^{+0.97}_{-0.68}) \times 10^{-5}$	$(2.32^{+0.35}_{-0.30}) \times 10^{-5}$
F_{tot} (erg cm $^{-2}$ s $^{-1}$)	$(8.65^{+1.64}_{-1.34}) \times 10^{-5}$	$(1.07^{+0.05}_{-0.05}) \times 10^{-4}$
$F_{\text{BB}}/F_{\text{tot}}$	$0.17^{+0.12}_{-0.08}$	$0.22^{+0.03}_{-0.03}$
S_{BB} (erg cm $^{-2}$)	$(1.52^{+0.98}_{-0.69}) \times 10^{-5}$	$(7.52^{+1.13}_{-0.99}) \times 10^{-5}$
S (erg cm $^{-2}$)	$(8.74^{+1.65}_{-1.35}) \times 10^{-5}$	$(3.48^{+0.27}_{-0.15}) \times 10^{-4}$
$L_{\text{BB},\gamma,\text{iso}}$ (erg s $^{-1}$)	$(7.28^{+4.67}_{-3.30}) \times 10^{51}$	$(1.12^{+0.17}_{-0.15}) \times 10^{52}$
$L_{\gamma,\text{iso}}$ (erg s $^{-1}$)	$(4.18^{+0.79}_{-0.65}) \times 10^{52}$	$(5.19^{+0.26}_{-0.23}) \times 10^{52}$
$E_{\text{BB},\gamma,\text{iso}}$ (erg)	$(7.36^{+4.72}_{-3.33}) \times 10^{51}$	$(3.63^{+0.55}_{-0.48}) \times 10^{52}$
$E_{\gamma,\text{iso}}$ (erg)	$(4.22^{+0.80}_{-0.63}) \times 10^{52}$	$(1.68^{+0.08}_{-0.07}) \times 10^{53}$
Photospheric properties		
Γ	741 ± 18	571 ± 12
r_0 (cm)	$(8.55 \pm 2.8) \times 10^6$	$(5.00 \pm 0.48) \times 10^7$
r_s (cm)	$(4.31 \pm 1.53) \times 10^9$	$(1.96 \pm 0.19) \times 10^{10}$
r_{ph} (cm)	$(5.33 \pm 0.47) \times 10^{11}$	$(1.41 \pm 0.04) \times 10^{12}$

Table 1: Comparison of properties between the two independent thermal emission episodes in GRB 190114C, which includes the observed and photospheric properties. For each thermal pulse, the table lists the durations; the best-fit parameters for the cut-off energy (E_c) and the temperature (kT), which are based on the CPL+BB model considering the time-integrated spectral analysis; the derived parameters, thermal F_{BB} and total F_{tot} energy flux; the averaged thermal flux ratio ($F_{\text{BB}}/F_{\text{tot}}$); the thermal (S_{BB}) and total (S) fluence, the averaged thermal ($L_{\text{BB},\gamma,\text{iso}}$) and total ($L_{\gamma,\text{iso}}$) luminosities; and the isotropic thermal ($E_{\text{BB},\gamma,\text{iso}}$) and total ($E_{\gamma,\text{iso}}$) energies, the bulk Lorentz factor Γ , the photospheric radius r_{ph} , saturation radius r_s , and nozzle radius r_0 .

	GRB 190114C- P_1^{th} (From $t_{\text{obs}} = 0.55$ s to 1.93 s)	GRB 190114C - P_2^{th} (From $t_{\text{obs}} = 2.45$ s to 5.69 s)
kT (keV)	$\propto t^{-0.93 \pm 0.04}$	$\propto t^{-1.32 \pm 0.09}$
\mathfrak{R} (cm)	$\propto t^{3.12 \pm 0.49}$	$\propto t^{2.37 \pm 0.32}$
Γ	$\propto t^{-0.48 \pm 0.05}$	$\propto t^{-0.81 \pm 0.08}$

Table 2: Power-law indices of the relevant parameters of two independent thermal pulses in GRB 190114C.

Measured quantities	
$E_{\text{th,iso}}$	$(6.46 \pm 0.53) \times 10^{52}$ erg
$E_{\text{nth,iso}}$	$(2.43 \pm 0.09) \times 10^{53}$ erg
F_{γ}^{obs}	$(1.01 \pm 0.03) \times 10^{-4}$ erg cm ⁻² s ⁻¹
$F_{\text{BB}}^{\text{obs}}$	$(1.86 \pm 0.24) \times 10^{-5}$ erg cm ⁻² s ⁻¹
t_{dec}	16.43 ± 0.07 s
kT^{obs}	144.4 ± 2.1 keV
z	0.4254 ± 0.0005
Derived parameters	
η	708 ± 8
Γ_{ph}	666 ± 6
Γ_0	507 ± 5
M_{iso}	$(8.6 \pm 0.6) \times 10^{-4} M_{\odot}$
$E_{\text{k,iso}}$	$(7.8 \pm 0.6) \times 10^{53}$ erg
$E_{\text{tot,iso}}$	$(1.1 \pm 0.1) \times 10^{54}$ erg
η_{γ}	$(28.3 \pm 1.4)\%$
$\epsilon_{e,-1}$	1.36 ± 0.03
$\epsilon_{\text{B},-2}$	0.09 ± 0.01
ν_{m}	$(1.85 \pm 0.15) \times 10^{17}$ Hz
ν_{c}	$(2.58 \pm 0.46) \times 10^{17}$ Hz
ν_{KN}	$(6.37 \pm 0.21) \times 10^{17}$ Hz

Table 3: The measured quantities from observations and the derived fireball parameters using our new methods (see Methods) with assuming $\mathcal{Y} = 1$ and $n = 1 \text{ cm}^{-3}$. The measured quantities include the isotropic equivalent thermal energy $E_{\text{th,iso}}$ and the non-thermal energy $E_{\text{nth,iso}}$, the total F_{γ}^{obs} and the thermal $F_{\text{BB}}^{\text{obs}}$ flux, the deceleration time t_{dec} , the average temperature kT^{obs} of the thermal component, and the redshift; the derived fireball parameters consist of the dimensionless specific enthalpy density at the engine η , the bulk Lorentz factor at the site of the photosphere Γ_{ph} , the initial afterglow Lorentz factor before the deceleration phase Γ_0 , the isotropic equivalent total mass M_{iso} , the kinetic energy in the fireball $E_{\text{k,iso}}$, and the γ -ray radiative efficiency η_{γ} , as well as the energy fractions assigned to electrons (ϵ_e) and magnetic (ϵ_{B}) fields, the characteristic synchrotron frequency (ν_{m}) and the cooling frequency (ν_{c}) of minimum-energy injected electrons, and the Klein-Nishina frequency (ν_{KN})

Methods

Uniqueness of Thermal Pulses of GRB 190114C GRB 190114C is unique in terms of the following aspects. (1) It has three well-separated emission episodes, which can be defined as the first, second, and third pulses. (2) The emission of the first two main pulses consists of two strong thermally-dominated episodes, which independently exhibit similar temporal properties. (3) The first two pulses (thermal) and the third pulse (non-thermal) have distinct spectral properties. (4) The thermal component has a thermal to total flux ratio of around 30%, which is the second highest among the GRBs observed with *Fermi*-GBM so far (the highest one is observed in GRB 090902B, with thermal flux ratio $\sim 70\%$). (5) Strong TeV emission was observed, setting the record of the highest photon energy in any GRB²⁷. The two well-separated pulses with independent and analogous thermal component evolution pattern make this extraordinarily bright GRB a unique event to study the jet composition and photospheric properties evolution in a single GRB. We note that in the cases of a hot fireball jet characterised by a quasi-thermal Planck-like spectrum (e.g. GRB 090902B⁴), a Poynting-flux-dominated outflow characterised by a Band (or cutoff power-law)-only function (e.g., GRB 080916C³³ and GRB 130427A³⁴), a hybrid jet characterised by either a two-component spectral scenario (composed of a non-thermal component and a thermal component simultaneously, e.g., GRB 110721A^{21,35}), or a transition from fireball to Poynting-flux-dominated outflow within a single GRB (e.g., GRB 160625B³⁶⁻³⁸), have been observed in the past. However, GRB 190114C presented unique information not available before.

Data Reduction We reduced the GBM data using a Python package, namely, *The Multi-Mission Maximum Likelihood Framework* (3ML³⁹). The data we used for our spectral analysis includes the two most strongly illuminated sodium iodide (NaI) scintillation detectors (n3, n4) and the most-illuminated bismuth germanium oxide (BGO) scintillation detector (b0) on board *Fermi*-GBM, as well as the corresponding response files (.rsp2 files are adopted). The detector selections were made considering to obtain an angle of incidence less than^{40,41} 60° for NaI and the lowest angle of incidence for BGO. The Time-Tagged Event (TTE) data type is used for the NaI data (8 keV–1 MeV) and BGO data (200 keV–40 MeV). In order to avoid the K-edge at 33.17 keV, the spectral energy range was also considered to cut from 30 to 40 keV. The background fitting is chosen using two off-source intervals, including the pre-burst (-20~ -10 s) and post-burst (180~200 s) epochs, and with the determined polynomial order (0-4) by applying a likelihood ratio test. The source interval is selected over the duration (-1~116 s) reported by the *Fermi*-GBM team. The maximum likelihood-based statistics, the so-called Pgstat, are used, given by a Poisson (observation)-Gaussian (background) profile likelihood⁴².

Bayesian Spectral Analysis The spectral parameters are obtained by adopting a fully Bayesian analysis approach. The main idea is that after the experimental data are obtained, Bayes's theorem is applied to infer and update the probability distribution of a specific set of model parameters. Building up a Bayesian profile model (M), and given an observed data set (D), the posterior probability distribution $p(M | D)$, according to the Bayes's theorem, is given by

$$p(M | D) = \frac{p(D | M)p(M)}{p(D)}, \quad (1)$$

where, $p(D | M)$ is the likelihood that combines the model and the observed data, and expresses the probability to observe (or generate) the dataset D from a given a model M with its parameters; $p(M)$ is the prior on the model parameters; and $p(D)$ is called the evidence, which is a constant with the purpose of normalisation. We utilise the typical spectral parameters from the *Fermi*-GBM catalogue as the prior distributions:

$$\left\{ \begin{array}{ll} A_{\text{Band}} \sim \log \mathcal{N} (\mu = 0, \sigma = 2) & \text{cm}^{-2} \text{keV}^{-1} \text{s}^{-1} \\ \alpha_{\text{Band}} \sim \mathcal{N} (\mu = -1, \sigma = 0.5) & \\ \beta_{\text{Band}} \sim \mathcal{N} (\mu = -2, \sigma = 0.5) & \\ E_{\text{Band}} \sim \log \mathcal{N} (\mu = 2, \sigma = 1) & \text{keV} \\ A_{\text{CPL}} \sim \log \mathcal{N} (\mu = 0, \sigma = 2) & \text{cm}^{-2} \text{keV}^{-1} \text{s}^{-1} \\ \alpha_{\text{CPL}} \sim \mathcal{N} (\mu = -1, \sigma = 0.5) & \\ E_{\text{CPL}} \sim \log \mathcal{N} (\mu = 2, \sigma = 1) & \text{keV} \\ A_{\text{BB}} \sim \log \mathcal{N} (\mu = -4, \sigma = 2) & \text{cm}^{-2} \text{keV}^{-1} \text{s}^{-1} \\ kT_{\text{BB}} \sim \log \mathcal{N} (\mu = 2, \sigma = 1) & \text{keV} \end{array} \right. \quad (2)$$

We employ a Markov Chain Monte Carlo (MCMC) sampling method (*emcee*⁴³) to sample the posterior. The parameter estimation is obtained at a maximum a posteriori probability from the Bayesian posterior density distribution, and its uncertainty (or the credible level) is evaluated from the Bayesian highest posterior density interval at 1σ (68%) Bayesian credible level.

Time-integrated and time-resolved Spectral Analysis We first perform the time-integrated spectral analysis (treating the entire T_{90} as one time bin, i.e., from T_0 to $T_0 + 116$ s) by using various GRB spectral models, including power-law (PL), cutoff power law (CPL), Band function⁴⁴, PL+blackbody (BB), CPL+BB, and Band+BB, respectively. The time-integrated spectral analysis suggests that the CPL+BB model can best characterise the spectral shape of the burst (see Sec. Model Comparison). The corresponding corner plot is shown in Figure 1 of the Extended Data.

GRB spectra are known to evolve over different pulses, or even within a pulse. The time-integrated spectral analysis, therefore, must be replaced by the time-resolved spectral analysis in order to study the GRB radiation mechanism in great detail. We first use the typical GRB spectral model, the Band model⁴⁴, to fit the time-resolved spectra in each slice (see Sec. BBlocks Methods). We found that the low-energy photon index α exhibits a wide-spread temporal variability (-0.14 to -1.99), and the majority of α values in the first two pulses are harder than the typical value of α defined by the synchrotron line of death ($\alpha=-2/3$)¹⁷, suggesting a significant contribution from thermal emission from the fireball photosphere^{3,20}. The majority of the high energy photon index β values are not well-constrained, indicating that the CPL model is preferred in comparison with the Band model. The violation of the synchrotron limit encourages us to search for an additional thermal component. In order to search for the best model to characterise the spectral shape of the burst, we attempt to fit the time-resolved spectra in each slice with both the CPL and the CPL+BB models. The DIC of the CPL+BB model is at least by 10 and can be hundreds less than the CPL model, indicating that adding a thermal component improves the spectral fitting greatly ($\Delta\text{DIC} > 10$, Ref.⁴⁵).

Model Comparison The best-fit model is reached by comparing the DIC values of different models and picking the one with the lowest value. The DIC is defined as $\text{DIC} = -2\log[p(\text{data}|\hat{\theta})] + 2p_{\text{DIC}}$, where $\hat{\theta}$ is the posterior mean of the parameters, and p_{DIC} is the effective number of parameters. The preferred model is the one that provides the lowest DIC score. We report the ΔDIC values by comparing the best model with other models in Table 1 in the Extended Data. Log(posterior) is adopted by the method of the maximum likelihood ratio test, which is treated as a reference of the model comparison⁴⁶.

BBlocks Methods We use a method called Bayesian blocks (BBlocks)⁴⁷ to rebin the Time Tagged Event (TTE) lightcurve. Time bins are selected in such a way as to capture the true variability of the data. Such a calculation requires each bin to be consistent with a constant Poisson rate. In each bin, it allows for a variable time width and signal-to-noise (S/N) ratio. We therefore apply the BBlocks method with the false alarm probability $p_0 = 0.01$ and the consideration of adequate significance to repartition the TTE lightcurve of the most strongly illuminated GBM detector (n4), other used detectors are binned in matching slices. We notice that the BBlocks analysis generates two slices (0.70 ~ 1.58 s and 1.58 ~ 1.71 s) from 0.70 s to 1.71 s. On the other hand, the two slices have a very high significance (263.97 and 115.59). In order to study the parameter evolution in great detail, we therefore rebin the time intervals with five narrower slices > 80 instead. We also did the same analysis on the last slice of P_2 (5.51 ~ 5.69 s), generating two narrower slices (5.51 ~ 5.65 s and 5.65 ~ 5.69 s), with the significance > 70 each, to study the temperature evolution in more detail. We therefore obtain 8 slices for P_1^{th} and 16 slices for P_2^{th} to study the photosphere properties.

Multi-wavelength Observations TeV (MAGIC) Observations:

The Major Atmospheric Gamma Imaging Cherenkov (MAGIC) telescopes observed for the first time very-high-energy gamma-ray (> 1 TeV) emission from T_0+57 s until $T_0+15912$ s²⁷, setting the record of the highest energy photon detected from any GRB. Both the TeV lightcurve and spectrum can be well-described by a power-law model¹, with the temporal decay index $\hat{\alpha}_{\text{MAGIC}} = 1.40 \pm 0.04$ and the spectral decay index $\hat{\beta}_{\text{MAGIC}} = 2.16 \pm 0.30$ (Figure 5 in the Extended Data). The total TeV-band (0.3-1 TeV) energy integrated between T_0+6 s and T_0+2454 s is $E_{\text{iso}}^{\text{MAGIC}} \sim 2.0 \times 10^{52}$ erg (Ref. 27).

GeV (Fermi-LAT) Observations: The first GeV photon was observed by *Fermi*-LAT at $T_0+2.1$ s. The highest-energy photon detected by LAT is a 22.9 GeV event detected at T_0+15 s⁴⁸. After that time, the lightcurve and spectrum as measured by LAT (0.1-100 GeV) from T_0+55 s to T_0+9975 s are well-fitted by a power-law model with the temporal decay index $\hat{\alpha}_{\text{LAT}} = 1.29 \pm 0.01$ and the spectral slope index $\hat{\beta}_{\text{LAT}} = -2.01 \pm 0.98$ (Figure 5 in the Extended Data). The total GeV-band (0.1-100 GeV) energy integrated between $T_0+2.1$ s and T_0+9975 s is $E_{\text{iso}}^{\text{LAT}} = (2.46 \pm 0.66) \times 10^{53}$ erg, which can be separated into two emission components: the prompt emission (≤ 15 s) accounts for $E_{\gamma,\text{iso}}^{\text{LAT}} = (4.60 \pm 0.69) \times 10^{52}$ erg, while the afterglow emission (> 15 s) accounts for $E_{\gamma,\text{iso}}^{\text{LAT}} = (2.00 \pm 0.59) \times 10^{53}$ erg.

¹The convention $F_{\nu,t} = t^{-\hat{\alpha}}\nu^{-\hat{\beta}}$ is adopted throughout the paper.

MeV (Fermi-GBM) Observations: Its duration (T_{90}) is about 116 s as reported by *Fermi*-GBM. The 1024 ms peak flux and the fluence at 10-1000 keV measured by *Fermi*-GBM are 246.9 ± 0.9 photon $\text{cm}^{-2} \text{s}^{-1}$ and $(4.436 \pm 0.005) \times 10^{-4}$ erg cm^{-2} , respectively. With a known redshift, $z=0.4245 \pm 0.0005$ (ref. ⁴⁹), the total k -corrected isotropic energy in the rest-frame 1-10⁴ keV band as derived from *Fermi*-GBM observations between T_0+0 s and T_0+116 s is $E_{\gamma,\text{iso}}=(3.12 \pm 0.10) \times 10^{53}$ (ref. ²⁸). The prompt emission (≤ 15 s) accounts for $E_{\gamma,\text{iso}}^{\text{GBM}} = (2.66 \pm 0.03) \times 10^{53}$ erg. There is a ~ 3.24 s lag between the GBM emission and the LAT emission.

keV (Swift-XRT) Observations: Following the trigger by *Swift*-BAT, the spacecraft slewed immediately to the location of the burst. The X-ray Telescope (XRT) began observing the afterglow at T_0+64 s. Pointed Windowed Timing mode data were collected from T_0+68 s to T_0+626 s, after which the count rate was low enough for Photon Counting mode to be utilised. The burst was followed for more than 28 days, although the last detection occurred on T_0+20 day. The XRT lightcurve showed a typical power-law behaviour with a power-law index $\hat{\alpha}_{\text{XRT}}=1.39 \pm 0.01$ (Figure 5 in the Extended Data). The isotropic X-ray energy release $E_{\text{XRT,iso}}$ measured by *Swift*-XRT (0.3-10 keV) from T_0+68 s to $T_0+13.86$ days is 2.11×10^{52} erg.

Optical Observations: Optical data have been gathered from refs. ^{27,50,51} as well as GCN data from refs. ⁵²⁻⁵⁹. The automatically processed UVOT data are also used. All afterglow data have been host-subtracted using the host-galaxy values taken from ref. ⁶⁰. Note that ref. ⁵⁰ found chromatic evolution in their early RINGO3 data. However, this effect is small, which leads to some additional scatter around the first steep-to-shallow decay transition. After the respective host galaxy magnitude has been subtracted for each band, all the bands are shifted to the R_c band to produce a composite lightcurve stretching from 33 s to 14.2 days after the GRB trigger. The lightcurve can be described by multiple power-law decay segments in a steep-shallow-steep arrangement. The first two segments have slopes $\hat{\alpha}_{\text{opt},1} = 2.076 \pm 0.023$ and $\hat{\alpha}_{\text{opt},2} = 0.544 \pm 0.011$, with a break time at $t_{b,1} = 0.00508 \pm 0.0003$ d and a smooth transition index with $n = -0.5$ (Figure 5 in the Extended Data). After a second, sharp break at $t_{b,2} = 0.576 \pm 0.028$ d, the lightcurve decays with $\hat{\alpha}_{\text{opt},3} = 1.067 \pm 0.011$. We find no evidence for a further break, in agreement with X-ray data, implying that the final slope seen in the data is either an unprecedentedly shallow post-jet-break decay slope (see the sample of ⁶¹ for comparison) or there is no jet break up to ≈ 10 d after the GRB trigger.

Deriving the Photosphere Properties Using the Traditional Method The thermal emission of GRB 190114C is extremely strong, ranking second in thermal-to-total flux ratio (30%) among the over 2700 GRBs observed by *Fermi*-GBM up to date (Figure 4 and Table 4 in the Extended Data). The identification of the strong thermal component in GRB 190114C allows us to determine the physical properties of the relativistic outflow within the framework of the non-dissipative photosphere theory^{22,62}. The photosphere photons observed at a given time, corresponding to one time bin in our time-resolved analysis, are assumed to be emitted from an independent thin shell. Therefore, the observed BB temperature kT_{obs} , the BB flux F_{BB} , and the total flux F_{tot} (thermal+non-thermal) of a given time bin determine the photosphere properties of the corresponding shell. The entire duration of photosphere emission is conjugated by the emissions from a sequence of such shells. One

can infer the bulk Lorentz factor Γ , and the initial size of the flow R_0 in each time bin and their temporal evolutions (Table 3 in the Extended Data).

The photosphere properties can be derived by considering the framework within the standard fireball model²². For a given shell, it is generated at an initial radius

$$r_0(r_{\text{ph}} > r_s) = \frac{4^{3/2}d_L}{(1.48)^6\xi^4(1+z)^2} \left(\frac{F_{\text{BB}}^{\text{obs}}}{Y F^{\text{obs}}} \right)^{3/2} \mathfrak{R}, \quad (3)$$

and self-accelerates to reach a saturated Lorentz factor

$$\eta(\equiv \Gamma)(r_{\text{ph}} > r_s) = \left[\xi(1+z)^2 d_L \left(\frac{Y F^{\text{obs}} \sigma_T}{2m_p c^3 \mathfrak{R}} \right) \right]^{1/4} \quad (4)$$

in the coasting phase. If the photosphere radius is greater than the saturation radius, it reads

$$r_{\text{ph}}(> r_s) = \frac{L_0 \sigma_T}{8\pi m_p c^3 \Gamma^3}, \quad (5)$$

where the dimensionless parameter

$$\mathfrak{R} = \left(\frac{F_{\text{BB}}}{\sigma_B T^4} \right)^{1/2} = \xi \frac{(1+z)^2 r_{\text{ph}}}{d_L \Gamma} \quad (6)$$

presents the effective transverse size of the photosphere. The burst luminosity $L_0 = 4\pi d_L^2 Y F_{\text{tot}}$ is given by the observation, Y is the ratio between the total fireball energy and the energy emitted in gamma-rays. The numerical factor ξ is of the order of unity that can be obtained from angular integration. The luminosity distance d_L of redshift z is integrated by assuming the standard Friedmann–Lemaître–Robertson–Walker (FLRW) metric. Other physical constants are the Thomson cross section σ_T , the proton rest mass m_p , the speed of light c , and the Stefan-Boltzmann constant σ_B .

Directly Deriving the Fireball Properties from Observations GRB 190114C has a redshift measurement. Its prompt emission is thermally dominated and its lightcurve has a clear early pulse indicating the afterglow initiation. These three properties make it the first case where one can use observational properties to directly determine the fireball characteristics including the dimensionless specific enthalpy density at the engine η , isotropic equivalent total mass M , bulk Lorentz factor at the site of the photosphere Γ_{ph} , initial afterglow Lorentz factor before the deceleration phase Γ_0 , the kinetic energy in the fireball E_k , and γ -ray radiative efficiency η_γ . The method described below follows Ref. ⁶.

The initial, total energy of a fireball is

$$E_{\text{tot}} = \eta M c^2. \quad (7)$$

The fireball undergoes rapid acceleration and reaches a Lorentz factor Γ_{ph} at the photosphere. The internal energy released as thermal emission can be estimated as

$$E_{\text{th}} = (\eta - \Gamma_{\text{ph}})Mc^2, \quad (8)$$

Afterwards, the fireball moves at an almost constant speed until internal dissipation at internal shocks occurs at a larger distance. The emitted non-thermal emission can be estimated as

$$E_{\text{nth}} = (\Gamma_{\text{ph}} - \Gamma_0)Mc^2, \quad (9)$$

where Γ_0 is the Lorentz factor after the dissipation and also the initial Lorentz factor in the afterglow phase.

The Lorentz factor at photosphere radius Γ_{ph} can be estimated as (modified from Ref.^{22,63}, see Ref.⁶ for details)

$$\Gamma_{\text{ph}} = \left[(1+z)^2 D_L \frac{\mathcal{Y} \sigma_T F_\gamma^{\text{obs}}}{2m_p c^3 \mathcal{R}} \frac{\eta^{3/2}}{\eta - \Gamma_0} \right]^{2/9}, \quad (10)$$

$$\mathcal{R} = \left(\frac{F_{\text{BB}}^{\text{obs}}}{\sigma_B T^4} \right)^{1/2}.$$

which involves several direct observables including redshift z , total flux F_γ^{obs} , thermal flux $F_{\text{BB}}^{\text{obs}}$ and the observed temperature T . Other parameters are the pair multiplicity parameter \mathcal{Y} which is commonly taken as 1, the luminosity distance D_L computed from the redshift adopting the FLRW cosmology, and fundamental constants such as speed of light c , proton mass m_p , Thomson cross section σ_T , and Stefan-Boltzmann constant σ_B .

The initial Lorentz factor of the afterglow phase Γ_0 can be derived by equating the kinetic energy to the swept-up ISM mass at the deceleration time t_{dec} , which is an observable indicated by a light-curve pulse (the third pulse for 190114C). Using Eq.(7.81) of ² and above arguments, we derive

$$\Gamma_0 \simeq 170 t_{\text{dec},2}^{-3/8} \left(\frac{1+z}{2} \right)^{3/8} \left(\frac{E_{\text{th},52} + E_{\text{nth},52}}{n} \right)^{1/8} \left(\frac{\Gamma_0}{\eta - \Gamma_0} \right)^{1/8}. \quad (11)$$

where n is the ISM density assumed as one particle per cubic centimetre as usual. The value of t_{dec} is determined in Figure 6.

Simultaneously solving Eqs. 8 – 11, we obtain fireball parameters η , Γ_{ph} , M and Γ_0 , and in turn. Then we can calculate the kinetic energy of the afterglow

$$E_k = \Gamma_0 M c^2, \quad (12)$$

and the efficiency of the prompt gamma-ray emission

$$\eta_\gamma = \frac{E_{\text{th}} + E_{\text{nth}}}{E_{\text{tot}}} = \frac{\eta - \Gamma_0}{\eta}. \quad (13)$$

Applying this to GRB 190114C, all the measured quantities are presented in the upper panel of Table 3, and all the derived parameters are presented in the lower panel of Table 3.

Further Estimate of the Energy Fractions Assigned to Electrons (ϵ_e) and Magnetic (ϵ_B) fields
Once E_k is precisely obtained from the observational data using our new methods discussed above, one can estimate the energy fractions assigned to electrons (ϵ_e) and magnetic (ϵ_B) fields using afterglow models (ref. ³⁰).

The isotropic blastwave kinetic energy ($E_{K,iso}$) can also be measured from the afterglow emission (normal decay) using the *Swift*-XRT data. For a constant density interstellar medium (ISM), the characteristic synchrotron frequency and the cooling frequency of minimum-energy injected electrons, and the peak spectral flux, therefore, can be given by^{30,64,65}

$$\nu_m = 3.3 \times 10^{12} \text{Hz} \left(\frac{p-2}{p-1} \right)^2 (1+z)^{1/2} \epsilon_{B,-2}^{1/2} \epsilon_{e,-1}^2 E_{K,iso,52}^{1/2} t_d^{-3/2}, \quad (14)$$

$$\nu_c = 6.3 \times 10^{15} \text{Hz} (1+z)^{-1/2} (1+Y)^{-2} \epsilon_{B,-2}^{-3/2} E_{K,iso,52}^{-1/2} n^{-1} t_d^{-1/2}, \quad (15)$$

$$F_{\nu,max} = 1.6 \text{mJy} (1+z) D_{28}^{-2} \epsilon_{B,-2}^{1/2} E_{K,iso,52} n^{-1}, \quad (16)$$

where p is the electron spectral distribution index, ϵ_e and ϵ_B are the energy fractions assigned to electrons and magnetic fields, t_d is the time in the observer frame in units of days, $D_{28} = D/10^{28}$, is the luminosity distance in units² of 10^{28} cm, n is the number density in the constant density ambient medium, and

$$Y = [-1 + (1 + 4\eta_1\eta_2\epsilon_e/\epsilon_B)^{1/2}] / 2, \quad (17)$$

is the Inverse Compton (IC) parameter, where $\eta_1 = \min[1, (\nu_c/\nu_m)^{(2-p)/2}]$, $\eta_2 = \min[1, (\nu_{KN}/\nu_c)^{(3-p)/2}]$ (for the slow cooling $\nu_m < \nu_x < \nu_c$ case) is a correction factor introduced by the Klein-Nishina effect, where ν_{KN} is the Klein-Nishina frequency

$$\nu_{KN} = h^{-1} \Gamma m_e c^2 \gamma_{e,X}^{-1} (1+z)^{-1} \simeq 2.4 \times 10^{15} \text{Hz} (1+z)^{-3/4} E_{K,iso,52}^{1/4} \epsilon_{B,-2}^{1/4} t_d^{-3/4} \nu_{18}^{-1/2}. \quad (18)$$

The spectral regime can be determined by using the closure relation in the afterglow emission via the observed temporal ($\hat{\alpha}$) and spectral ($\hat{\beta}$) indices. The temporal index $\hat{\alpha}_{\text{XRT}}$ is measured from the *Swift*-XRT lightcurve (see Figure 5), and the corresponding spectral index $\hat{\beta}_{\text{XRT}} = -(\Gamma_{\text{XRT}} - 1) = -0.93 \pm 0.10$ (Γ_{XRT} is the photon spectral index) is available from the *Swift* online server^{66,67}. Using the temporal and spectral indices, one can therefore determine that the X-ray emission in GRB 190114C is in the $\nu_m < \nu_x < \nu_c$ regime. With the spectral regime known, the electron index p can be derived using the observed temporal index: $p = (3 - 4\hat{\alpha}_{\text{XRT}})/3 = 2.85 \pm 0.01$.

In the case of $p > 2$, and in the $\nu_m < \nu_x < \nu_c$ regime, one can derive the X-ray band energy flux as

$$\begin{aligned} \nu F_\nu(\nu = 10^{18} \text{Hz}) &= F_{\nu,max} (\nu_m/\nu_x)^{(p-1)/2} \\ &= 6.5 \times 10^{-13} \text{ergs}^{-1} \text{cm}^{-2} D_{28}^{-2} (1+z)^{(p+3)/4} \\ &\times f_p \epsilon_{B,-2}^{(p+1)/4} \epsilon_{e,-1}^{p-1} E_{K,iso,52}^{(p+3)/4} n^{1/2} t_d^{(3-3p)/4} \nu_{18}^{(3-p)/2}. \end{aligned} \quad (19)$$

²The convention $Q = 10^x Q_x$ is adopted in cgs units for all parameters throughout the paper.

This gives,

$$\begin{aligned}
E_{\text{K,iso},52} = & \left[\frac{\nu F_\nu(\nu = 10^{18}\text{Hz})}{6.5 \times 10^{-13}\text{ergs}^{-1}\text{cm}^{-2}} \right]^{4/(p+3)} \\
& \times D_{28}^{8/(p+3)} (1+z)^{-1} t_d^{3(p-1)/(p+3)} \\
& \times f_p^{-4/(p+3)} \epsilon_{B,-2}^{-(p+1)/(p+3)} \epsilon_{e,-1}^{4(1-p)/(p+3)} \\
& \times n^{-2/(p+3)} \nu_{18}^{2(p-3)/(p+3)},
\end{aligned} \tag{20}$$

where $\nu F_\nu(\nu = 10^{18})$ Hz is the energy flux at frequency 10^{18} Hz in units of $\text{erg s}^{-1} \text{cm}^{-2}$, and

$$f_p = 6.73 \left(\frac{p-2}{p-1} \right)^{p-1} (3.3 \times 10^{-6})^{(p-2.3)/2}. \tag{21}$$

is a function of the electron power-law index p .

Simultaneously solving Eq. 17 and Eq. 20, with the IC parameter Y constrained from the observations in GRB 190114C, e.g. $Y = E_{\text{GeV}}/E_{\text{MeV}}=0.75$, we obtain ϵ_B and ϵ_e ,

$$\begin{cases} \epsilon_{e,-1} = 1.36 \pm 0.03, \\ \epsilon_{B,-2} = 0.09 \pm 0.01, \end{cases} \tag{22}$$

With known the values of ϵ_B and ϵ_e , we can also solve for ν_m , ν_c , and ν_{KN} ,

$$\begin{cases} \nu_m = (1.85 \pm 0.15) \times 10^{17}\text{Hz}, \\ \nu_c = (2.58 \pm 0.46) \times 10^{17}\text{Hz}, \\ \nu_{\text{KN}} = (6.37 \pm 0.21) \times 10^{17}\text{Hz} \end{cases} \tag{23}$$

References

33. Abdo, A. A. *et al.* Fermi Observations of High-Energy Gamma-Ray Emission from GRB 080916C. *Science* **323**, 1688– (2009).
34. Preece, R. *et al.* Which E_{peak} ? The Characteristic Energy of Gamma-ray Burst Spectra. *The Astrophysical Journal* **821**, 12 (2016). 1603.02962.
35. Gao, H. & Zhang, B. Photosphere Emission from a Hybrid Relativistic Outflow with Arbitrary Dimensionless Entropy and Magnetization in GRBs. *The Astrophysical Journal* **801**, 103 (2015). 1409.3584.
36. Ryde, F. *et al.* Observational evidence of dissipative photospheres in gamma-ray bursts. *Monthly Notices of the Royal Astronomical Society* **415**, 3693–3705 (2011). 1103.0708.
37. Zhang, B.-B. *et al.* Transition from fireball to Poynting-flux-dominated outflow in the three-episode GRB 160625B. *Nature Astronomy* **2**, 69–75 (2018). 1612.03089.
38. Li, L. Multipulse Fermi Gamma-Ray Bursts. I. Evidence of the Transition from Fireball to Poynting-flux-dominated Outflow. *The Astrophysical Journals* **242**, 16 (2019). 1810.03129.
39. Vianello, G. *et al.* The Multi-Mission Maximum Likelihood framework (3ML). *arXiv e-prints* (2015). 1507.08343.
40. Goldstein, A. *et al.* The Fermi GBM Gamma-Ray Burst Spectral Catalog: The First Two Years. *The Astrophysical Journals* **199**, 19 (2012). 1201.2981.
41. Narayana Bhat, P. *et al.* The Third Fermi GBM Gamma-Ray Burst Catalog: The First Six Years. *The Astrophysical Journals* **223**, 28 (2016). 1603.07612.
42. Cash, W. Parameter estimation in astronomy through application of the likelihood ratio. *ApJ* **228**, 939–947 (1979).
43. Foreman-Mackey, D., Hogg, D. W., Lang, D. & Goodman, J. emcee: The MCMC Hammer. **125**, 306 (2013). 1202.3665.
44. Band, D. *et al.* BATSE observations of gamma-ray burst spectra. I - Spectral diversity. *The Astrophysical Journal* **413**, 281–292 (1993).
45. Acuner, Z., Ryde, F., Pe’er, A., Mortlock, D. & Ahlgren, B. The Fraction of Gamma-Ray Bursts with an Observed Photospheric Emission Episode. *The Astrophysical Journal* **893**, 128 (2020). 2003.06223.
46. Vuong, Q. H. Likelihood ratio tests for model selection and non-nested hypotheses. *Econometrica* **57**, 307–333 (1989). URL <http://www.jstor.org/stable/1912557>.

47. Scargle, J. D., Norris, J. P., Jackson, B. & Chiang, J. Studies in Astronomical Time Series Analysis. VI. Bayesian Block Representations. *The Astrophysical Journal* **764**, 167 (2013). 1207.5578.
48. Kocevski, D. *et al.* GRB 190114C: Fermi-LAT detection. *GRB Coordinates Network, Circular Service, No. 23709, #1 (2019/January-0)* **23709** (2019).
49. Selsing, J., Fynbo, J. P. U., Heintz, K. E. & Watson, D. GRB 190114C: NOT optical counterpart and redshift. *GRB Coordinates Network* **23695**, 1 (2019).
50. Jordana-Mitjans, N. *et al.* Lowly Polarized Light from a Highly Magnetized Jet of GRB 190114C. *The Astrophysical Journal* **892**, 97 (2020). 1911.08499.
51. Misra, K. *et al.* Low frequency view of GRB 190114C reveals time varying shock microphysics. *Monthly Notices of the Royal Astronomical Society* **submitted (arXiv:1911.09719)**, arXiv:1911.09719 (2019). 1911.09719.
52. Bikmaev, I. *et al.* GRB 190114C: RTT150 optical observations. *GRB Coordinates Network* **23766**, 1 (2019).
53. Im, M., Paek, G. S., Kim, S., Lim, G. & Choi, C. GRB 190114C: Optical observations. *GRB Coordinates Network* **23717**, 1 (2019).
54. Im, M., Paek, G. S. H. & Choi, C. GRB 190114C: UKIRT JHK observation (CORRECTIONS). *GRB Coordinates Network* **23757**, 1 (2019).
55. Kim, J. & Im, M. GRB 190114C: LSGT optical observation. *GRB Coordinates Network* **23732**, 1 (2019).
56. Kim, J. *et al.* GRB 190114C: KMTNet optical observation. *GRB Coordinates Network* **23734**, 1 (2019).
57. Mazaeva, E., Pozanenko, A., Volnova, A., Belkin, S. & Krugov, M. GRB 190114C: CHILESCOPE optical observations. *GRB Coordinates Network* **23741**, 1 (2019).
58. Watson, A. M. *et al.* GRB 190114C: COATLI Optical Detection. *GRB Coordinates Network* **23749**, 1 (2019).
59. Watson, A. M. *et al.* GRB 190114C: RATIR Optical and NIR Detections. *GRB Coordinates Network* **23751**, 1 (2019).
60. de Ugarte Postigo, A. *et al.* GRB 190114C in the nuclear region of an interacting galaxy. A detailed host analysis using ALMA, the HST, and the VLT. **633**, A68 (2020). 1911.07876.
61. Zeh, A., Klose, S. & Kann, D. A. Gamma-Ray Burst Afterglow Light Curves in the Pre-Swift Era: A Statistical Study. *The Astrophysical Journal* **637**, 889–900 (2006). astro-ph/0509299.

62. Vereshchagin, G. V. & Aksenov, A. G. *Relativistic kinetic theory: with applications in astrophysics and cosmology* (Cambridge University Press, 2017).
63. Bégué, D. & Iyyani, S. Transparency Parameters from Relativistically Expanding Outflows. *The Astrophysical Journal* **792**, 42 (2014).
64. Sari, R., Piran, T. & Narayan, R. Spectra and Light Curves of Gamma-Ray Burst Afterglows. *The Astrophysical Journal Letters* **497**, L17–L20 (1998). astro-ph/9712005.
65. Yost, S. A., Harrison, F. A., Sari, R. & Frail, D. A. A Study of the Afterglows of Four Gamma-Ray Bursts: Constraining the Explosion and Fireball Model. *The Astrophysical Journal* **597**, 459–473 (2003). astro-ph/0307056.
66. Evans, P. A. *et al.* An online repository of Swift/XRT light curves of γ -ray bursts. **469**, 379–385 (2007). 0704.0128.
67. Evans, P. A. *et al.* Methods and results of an automatic analysis of a complete sample of Swift-XRT observations of GRBs. *Monthly Notices of the Royal Astronomical Society* **397**, 1177–1201 (2009). 0812.3662.

Extended Data

Extended Data Figure 1: **Bayesian Monte Carlo fitting of *Fermi*-GBM T_{90} spectrum from 0 s to 116 s**

Extended Data Figure 2: **Temporal evolution of the parameter \mathfrak{R} .**

Extended Data Figure 3: **Temporal evolution of the photospheric radius r_{ph} , saturation radius r_s , and nozzle radius r_0 .**

Extended Data Figure 4: **Temporal evolution of the BB energy flux and total energy flux (left panel). The total energy flux versus the BB energy flux (right panel).**

Extended Data Figure 5: **multi-wavelength lightcurve (left panel) and multi-wavelength spectrum (right panel).**

Extended Data Figure 6: **The count GBM lightcurve (black) with the best fitting (purple line) to the third pulse using the FRED model.**

Extended Data Table 1: **Comparison of ΔDIC between the best model to other various models, which is based on the time-integrated spectral analysis.**

Extended Data Table 2: **Spectral parameters of the slices having a thermal component in GRB 190114C.**

Extended Data Table 3: **Photosphere properties of the slices having a thermal component in GRB 190114C.**

Extended Data Table 4: **Time-resolved spectral fit results of GRB 190114C.**

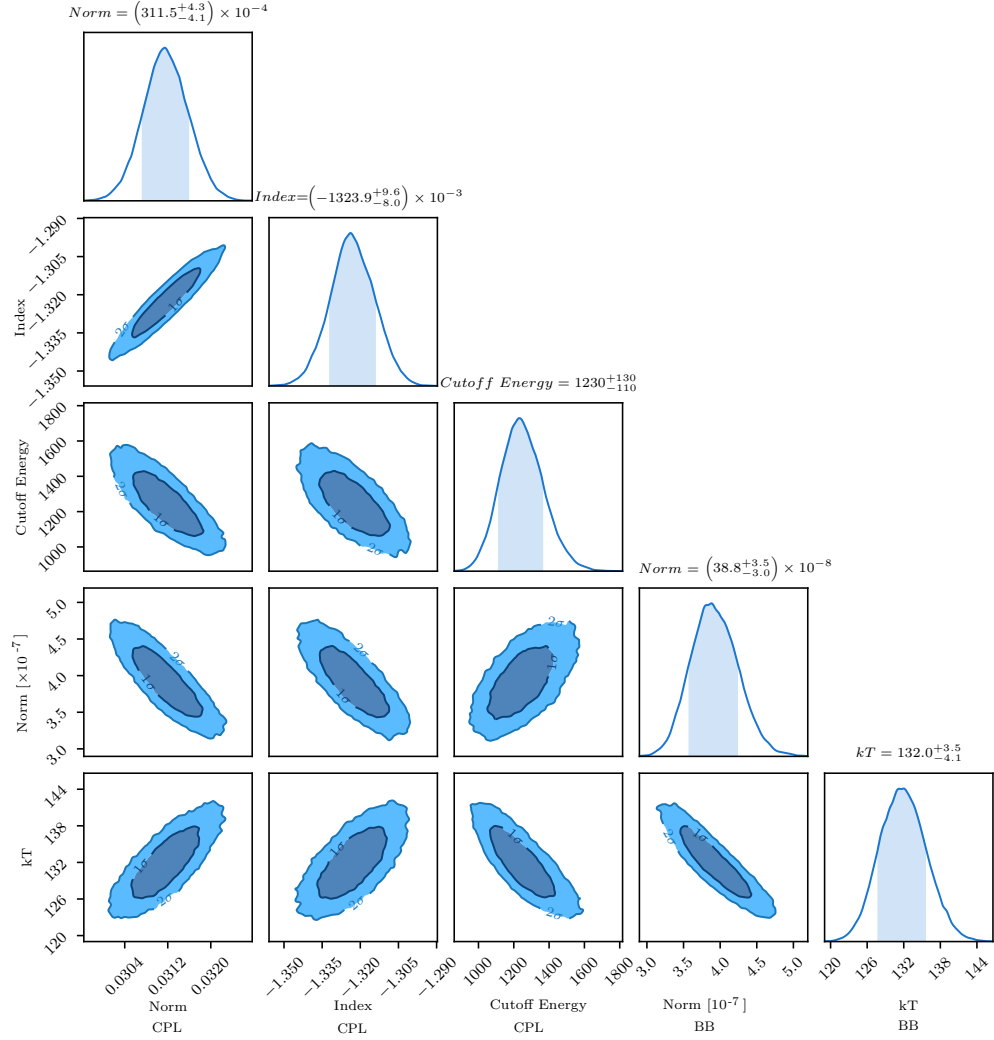


Figure 1: Bayesian Monte Carlo fitting of the *Fermi*-GBM spectrum from 0 s to 116 s (T_{90}). We apply 20 chains, each chain iterates 10^4 times and burns the first 10^3 times. The parameters are normalisation (Norm CPL), cut-off energy and power-law index of the cut-off power-law model, as well as normalisation (Norm BB) and temperature (kT) of the BB model.

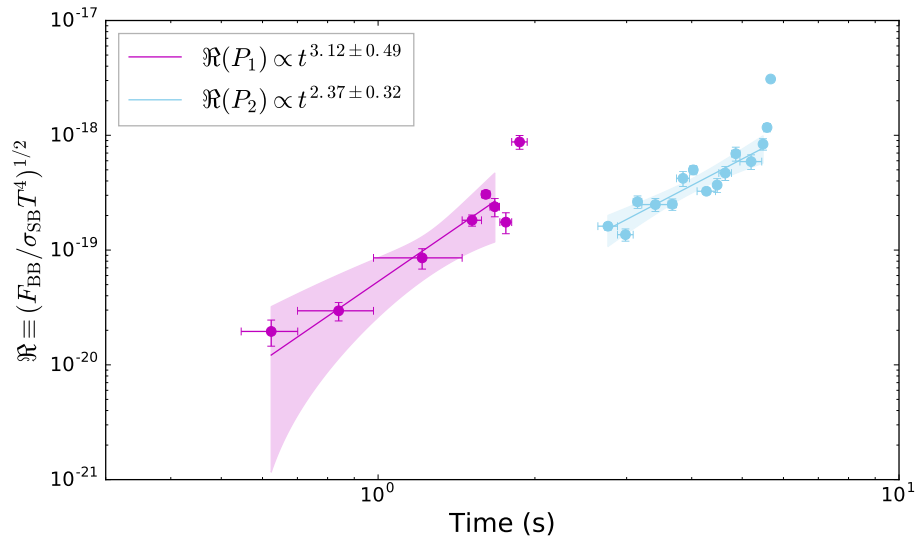


Figure 2: Temporal evolution of the parameter \mathfrak{R} . Same color notation as in Fig. 2.

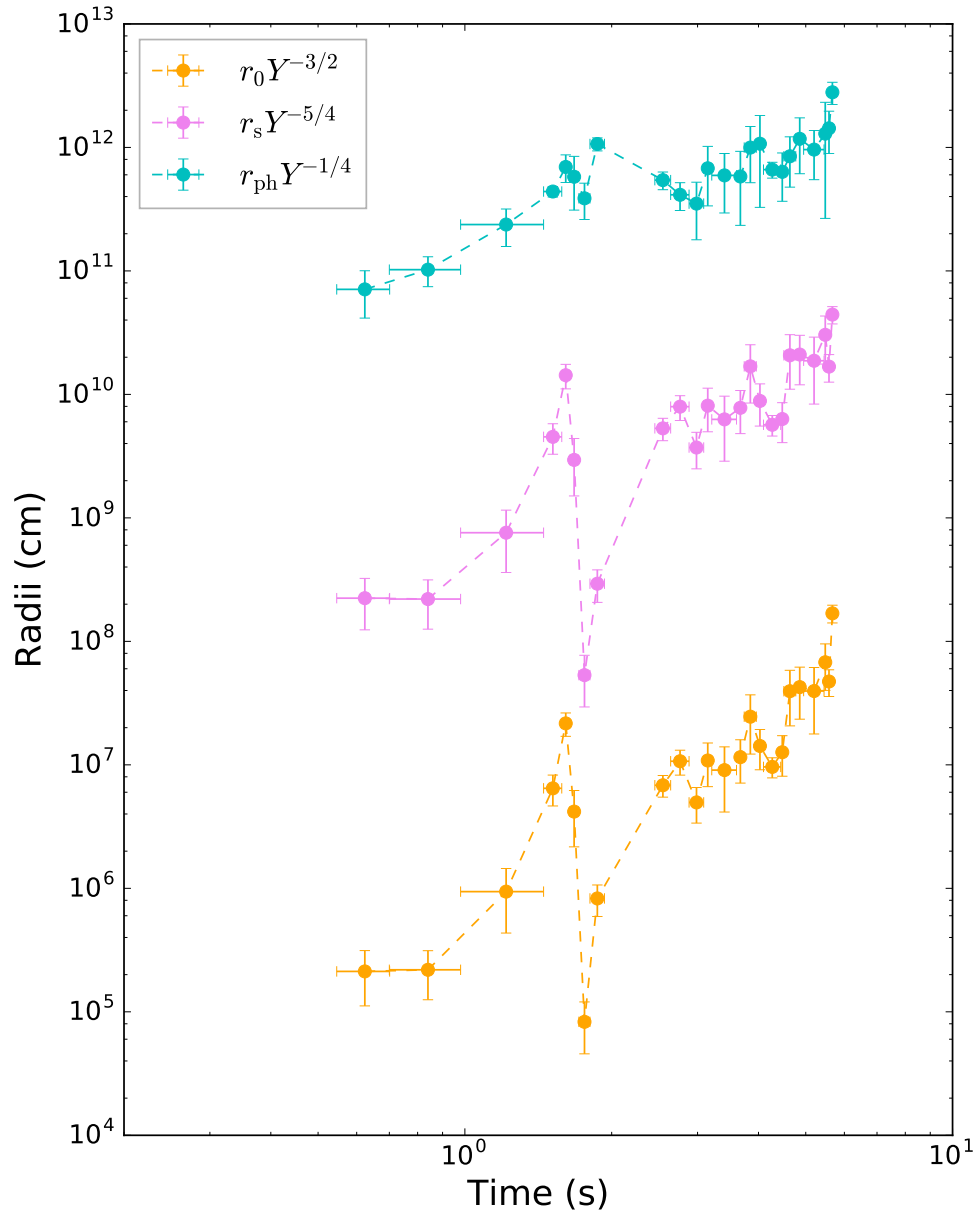


Figure 3: Temporal evolution of the photospheric radius r_{ph} , saturation radius r_s , and nozzle radius r_0 . Different colours represent different characteristic radii: r_0 (orange), r_s (violet), and r_{ph} (cyan).

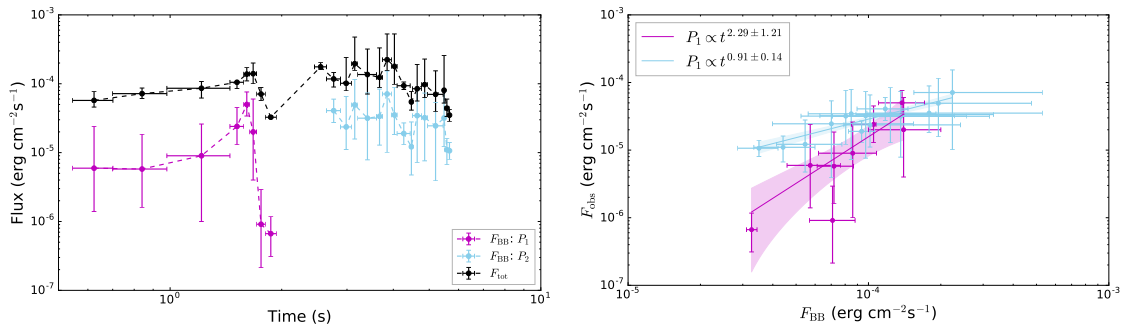


Figure 4: Temporal evolution of the BB energy flux and total energy flux (left panel). The total energy flux versus the BB energy flux (right panel). Same color notation as in Fig. 2.

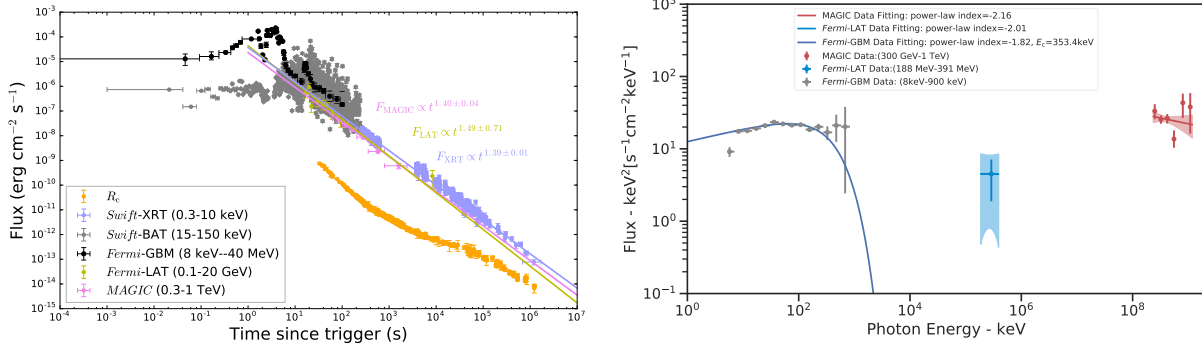


Figure 5: Left panel: multi-wavelength lightcurve. The data points indicated by violet, yellow, black, grey, purple, and orange represent the MAGIC, *Fermi*-LAT, *Fermi*-GBM, *Swift*-BAT, *Swift*-XRT, and the optical observations, respectively. The solid lines are the best power-law fitting to the data. Note that: (1) The LAT data are separated into two part at ~ 15 s, and here we only fit the second (afterglow) part (>15 s). (2) The optical Rc-band has been corrected for Galactic and host extinction, and the contribution from the host galaxy has also been subtracted. This lightcurve has been created by shifting data from different bands to the R band (see Methods). Right panel: multi-wavelength spectrum covering the energy in MeV, GeV, and TeV emission, which is simultaneously observed from T_0+68 s to T_0+110 s by *Fermi*-GBM, *Fermi*-LAT, and MAGIC, respectively

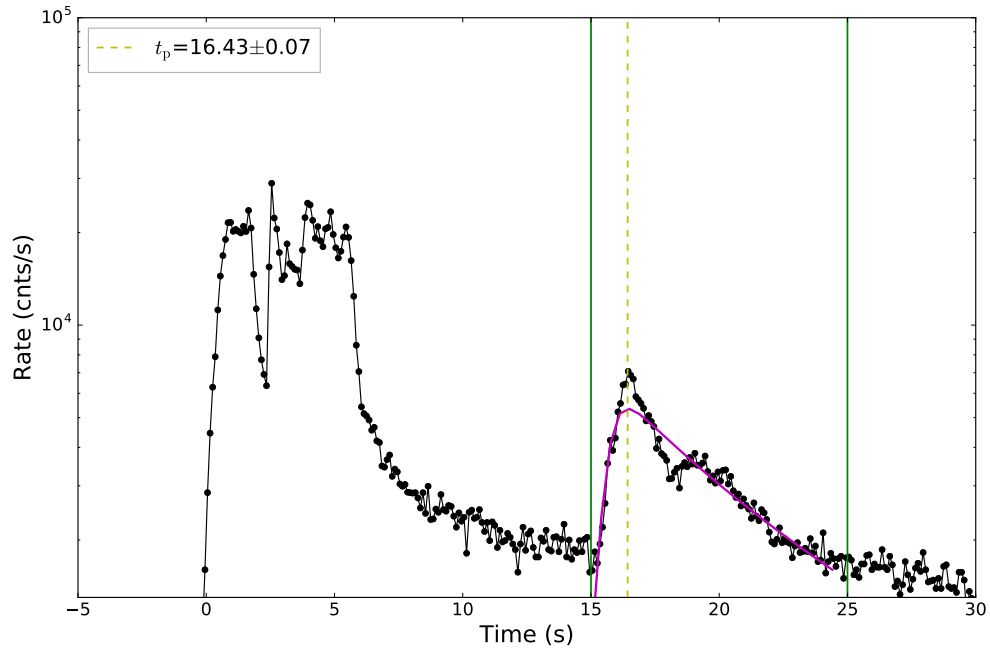


Figure 6: The GBM count lightcurve (black) with the best fitting (purple line) to the third pulse using the FRED model. The value of t_p is used to estimate Γ in equation (11).

	$t_1 \sim t_2$ (s)	$\Delta\text{DIC}(1)$ (CPL+BB)-(PL)	$\Delta\text{DIC}(2)$ (CPL+BB)-(BB)	$\Delta\text{DIC}(3)$ (CPL+BB)-(CPL)	$\Delta\text{DIC}(4)$ (CPL+BB)-(Band)	$\Delta\text{DIC}(5)$ (CPL+BB)-(PL+BB)
GRB 190114C	0~116	-3523	-19565	-266	-262	-457

Table 1: Comparison of ΔDIC between the best model and other various models, which is based on the time-integrated spectral analysis.

	$t_{\text{start}} \sim t_{\text{stop}}$ (s)	S	Model	ΔDIC $\text{DIC}_{(\text{CPL+BB})-(\text{CPL})}$	Temperature (keV)	Thermal Flux ($\text{erg cm}^{-2} \text{ s}^{-1}$)	Total Flux ($\text{erg cm}^{-2} \text{ s}^{-1}$)	Ratio
P_1^{th}	0.55~0.70	96.49	CPL+BB	-176.5	$350.7_{-99.9}^{+98.5}$	$0.59_{-0.45}^{+1.82} \times 10^{-5}$	$0.57_{-0.11}^{+0.19} \times 10^{-4}$	$0.10_{-0.08}^{+0.32}$
	0.70~0.98	153.65	CPL+BB	-285.1	$283.1_{-55.1}^{+59.2}$	$0.58_{-0.42}^{+1.27} \times 10^{-5}$	$0.72_{-0.11}^{+0.15} \times 10^{-4}$	$0.08_{-0.06}^{+0.18}$
	0.98~1.45	196.39	CPL+BB	-42.6	$186.2_{-34.4}^{+40.2}$	$0.91_{-0.80}^{+1.72} \times 10^{-5}$	$0.86_{-0.24}^{+0.22} \times 10^{-4}$	$0.10_{-0.10}^{+0.20}$
	1.45~1.58	105.17	CPL+BB	-148.0	$163.0_{-19.0}^{+20.0}$	$2.42_{-1.13}^{+2.10} \times 10^{-5}$	$1.05_{-0.20}^{+0.03} \times 10^{-4}$	$0.23_{-0.11}^{+0.20}$
	1.58~1.64	80.78	CPL+BB	-29.0	$151.0_{-11.0}^{+11.0}$	$5.26_{-1.69}^{+2.68} \times 10^{-5}$	$1.38_{-0.28}^{+0.33} \times 10^{-4}$	$0.36_{-0.14}^{+0.21}$
	1.64~1.71	83.47	CPL+BB	-21.2	$136.0_{-24.0}^{+28.0}$	$2.06_{-1.63}^{+4.18} \times 10^{-5}$	$1.49_{-0.41}^{+0.68} \times 10^{-4}$	$0.14_{-0.12}^{+0.29}$
	1.71~1.80	88.47	CPL+BB	-113.7	$73.3_{-17.8}^{+13.2}$	$0.09_{-0.07}^{+0.20} \times 10^{-5}$	$0.71_{-0.14}^{+0.17} \times 10^{-4}$	$0.01_{-0.01}^{+0.03}$
	1.80~1.93	80.82	CPL+BB	-138.6	$30.3_{-4.7}^{+4.3}$	$0.07_{-0.04}^{+0.05} \times 10^{-5}$	$0.32_{-0.02}^{+0.02} \times 10^{-4}$	$0.02_{-0.01}^{+0.02}$
P_2^{th}	2.45~2.64	152.16	CPL+BB	-20.6	$173.9_{-12.6}^{+13.1}$	$3.88_{-1.40}^{+1.89} \times 10^{-5}$	$1.76_{-0.24}^{+0.26} \times 10^{-4}$	$0.22_{-0.09}^{+0.11}$
	2.64~2.88	136.19	CPL+BB	-622.0	$197.4_{-16.4}^{+16.5}$	$4.07_{-1.34}^{+1.91} \times 10^{-5}$	$1.17_{-0.28}^{+0.28} \times 10^{-4}$	$0.35_{-0.14}^{+0.18}$
	2.88~3.09	103.16	CPL+BB	-12.4	$187.6_{-21.9}^{+21.5}$	$2.36_{-1.11}^{+1.83} \times 10^{-5}$	$1.01_{-0.29}^{+0.38} \times 10^{-4}$	$0.23_{-0.13}^{+0.20}$
	3.09~3.21	92.86	CPL+BB	-19.7	$162.1_{-7.6}^{+12.2}$	$4.93_{-1.58}^{+1.71} \times 10^{-5}$	$1.95_{-0.57}^{+0.85} \times 10^{-4}$	$0.25_{-0.11}^{+0.14}$
	3.21~3.60	146.18	CPL+BB	-36.7	$149.2_{-7.6}^{+7.4}$	$3.16_{-0.79}^{+1.03} \times 10^{-5}$	$1.36_{-0.31}^{+0.47} \times 10^{-4}$	$0.23_{-0.08}^{+0.11}$
	3.60~3.74	82.69	CPL+BB	-20.0	$151.0_{-11.1}^{+11.2}$	$3.36_{-1.28}^{+1.65} \times 10^{-5}$	$1.23_{-0.49}^{+0.84} \times 10^{-4}$	$0.27_{-0.15}^{+0.23}$
	3.74~3.96	140.29	CPL+BB	-62.7	$140.4_{-4.5}^{+4.6}$	$7.11_{-1.01}^{+1.13} \times 10^{-5}$	$2.23_{-0.55}^{+0.81} \times 10^{-4}$	$0.32_{-0.09}^{+0.13}$
	3.96~4.10	130.66	CPL+BB	-44.0	$108.2_{-7.0}^{+5.7}$	$3.52_{-1.83}^{+1.85} \times 10^{-5}$	$1.79_{-0.79}^{+1.71} \times 10^{-4}$	$0.20_{-0.13}^{+0.22}$
	4.10~4.44	170.04	CPL+BB	-921.9	$114.8_{-7.2}^{+7.0}$	$1.89_{-0.59}^{+0.80} \times 10^{-5}$	$0.94_{-0.11}^{+0.13} \times 10^{-4}$	$0.20_{-0.07}^{+0.09}$
	4.44~4.51	69.23	CPL+BB	-207.4	$96.6_{-13.2}^{+14.8}$	$1.22_{-0.74}^{+1.57} \times 10^{-5}$	$0.55_{-0.13}^{+0.23} \times 10^{-4}$	$0.22_{-0.15}^{+0.30}$
	4.51~4.77	142.52	CPL+BB	-132.9	$111.1_{-5.0}^{+5.1}$	$3.45_{-0.72}^{+1.02} \times 10^{-5}$	$0.85_{-0.16}^{+0.22} \times 10^{-4}$	$0.41_{-0.12}^{+0.16}$
	4.77~4.95	134.52	CPL+BB	-53.9	$89.9_{-4.0}^{+3.9}$	$3.21_{-0.76}^{+0.89} \times 10^{-5}$	$0.97_{-0.23}^{+0.33} \times 10^{-4}$	$0.33_{-0.11}^{+0.15}$
	4.95~5.45	184.46	CPL+BB	-176.2	$91.0_{-2.7}^{+2.7}$	$2.45_{-0.39}^{+0.45} \times 10^{-5}$	$0.70_{-0.10}^{+0.14} \times 10^{-4}$	$0.35_{-0.07}^{+0.09}$
	5.45~5.51	76.02	CPL+BB	-92.9	$81.5_{-4.9}^{+5.4}$	$3.18_{-1.22}^{+1.30} \times 10^{-5}$	$0.80_{-0.32}^{+0.95} \times 10^{-4}$	$0.40_{-0.22}^{+0.49}$
5.51~5.65	100.84	CPL+BB	-26.5	$52.9_{-3.5}^{+3.6}$	$1.10_{-0.43}^{+0.51} \times 10^{-5}$	$0.44_{-0.16}^{+0.11} \times 10^{-4}$	$0.25_{-0.12}^{+0.13}$	
5.65~5.69	48.93	CPL+BB	-25.8	$32.3_{-1.63}^{+1.68}$	$1.07_{-0.26}^{+0.33} \times 10^{-5}$	$0.35_{-0.06}^{+0.07} \times 10^{-4}$	$0.30_{-0.09}^{+0.11}$	
T_{90}	0.00~116.00	190.61	CPL+BB	-266.1	$135.0_{-4.1}^{+4.1}$	$0.14_{-0.02}^{+0.02} \times 10^{-5}$	$0.05_{-0.00}^{+0.00} \times 10^{-4}$	$0.31_{-0.05}^{+0.06}$

Table 2: Spectral parameters of the slices having a thermal component in GRB 190114C. The spectra are best fitted by a two-component scenario, with a thermal BB component accompanied by a non-thermal CPL component. The table lists the start and stop times of the BB blocks slices, the significance, the best-fitted model, the ΔDIC between CPL+BB and CPL models, the temperature, the thermal and total flux, and the ratio of thermal flux. Flux is defined in the energy band of 1 keV to 10 MeV. For the slices of ~ 3 s to ~ 4 s, Band+BB offers a very close goodness of fitting as CPL+BB, for the global consistency, and considering the time-integrated spectrum is best fitted by CPL+BB, here we perform all the thermal analysis using CPL+BB.

	$t_{\text{start}} \sim t_{\text{stop}}$	\mathfrak{R}	Γ	r_0	r_s	r_{ph}
	(s)	(10^{-19})		(10^7 cm)	(10^{10} cm)	(10^{12} cm)
P_1^{th}	0.55~0.70	0.20 ± 0.05	1053 ± 78	0.02 ± 0.01	0.02 ± 0.01	0.07 ± 0.03
	0.70~0.98	0.30 ± 0.05	1005 ± 49	0.02 ± 0.01	0.02 ± 0.01	0.10 ± 0.03
	0.98~1.45	0.86 ± 0.18	806 ± 50	0.09 ± 0.05	0.08 ± 0.04	0.24 ± 0.08
	1.45~1.58	1.82 ± 0.20	702 ± 21	0.65 ± 0.17	0.45 ± 0.12	0.44 ± 0.04
	1.58~1.64	3.06 ± 0.22	660 ± 16	2.17 ± 0.44	1.43 ± 0.30	0.69 ± 0.17
	1.64~1.71	2.38 ± 0.46	705 ± 40	0.42 ± 0.21	0.29 ± 0.16	0.58 ± 0.28
	1.71~1.80	1.75 ± 0.39	642 ± 40	0.01 ± 0.00	0.01 ± 0.00	0.39 ± 0.12
	1.80~1.93	8.75 ± 1.21	354 ± 13	0.08 ± 0.03	0.03 ± 0.01	1.07 ± 0.12
P_2^{th}	2.45~2.64	2.03 ± 0.15	777 ± 16	0.68 ± 0.14	0.53 ± 0.11	0.54 ± 0.08
	2.64~2.88	1.61 ± 0.13	744 ± 22	1.07 ± 0.25	0.80 ± 0.18	0.41 ± 0.11
	2.88~3.09	1.36 ± 0.16	748 ± 27	0.50 ± 0.16	0.37 ± 0.12	0.35 ± 0.17
	3.09~3.21	2.64 ± 0.31	747 ± 26	1.08 ± 0.42	0.81 ± 0.30	0.68 ± 0.35
	3.21~3.60	2.49 ± 0.34	692 ± 37	0.91 ± 0.46	0.63 ± 0.31	0.59 ± 0.30
	3.60~3.74	2.50 ± 0.29	675 ± 26	1.15 ± 0.42	0.78 ± 0.27	0.58 ± 0.35
	3.74~3.96	4.22 ± 0.62	687 ± 31	2.46 ± 1.16	1.69 ± 0.83	1.00 ± 0.51
	3.96~4.10	5.00 ± 0.48	623 ± 28	1.42 ± 0.54	0.89 ± 0.33	1.07 ± 0.73
	4.10~4.44	3.26 ± 0.21	590 ± 11	0.96 ± 0.17	0.57 ± 0.10	0.66 ± 0.09
	4.44~4.51	3.69 ± 0.51	499 ± 21	1.27 ± 0.45	0.63 ± 0.23	0.63 ± 0.28
	4.51~4.77	4.69 ± 0.67	525 ± 24	3.95 ± 1.97	2.07 ± 1.02	0.85 ± 0.38
	4.77~4.95	6.91 ± 0.93	493 ± 23	4.26 ± 1.96	2.10 ± 0.96	1.17 ± 0.58
	4.95~5.45	5.90 ± 0.87	473 ± 24	3.96 ± 2.09	1.87 ± 1.03	0.96 ± 0.41
	5.45~5.51	8.38 ± 0.94	448 ± 18	6.77 ± 2.69	3.04 ± 1.22	1.29 ± 0.99
	5.51~5.65	11.70 ± 0.94	355 ± 10	4.73 ± 1.20	1.68 ± 0.43	1.43 ± 0.56
5.65~5.69	30.92 ± 1.61	263 ± 5	16.86 ± 2.75	4.43 ± 0.76	2.80 ± 0.59	

Table 3: Photosphere properties of the slices having a thermal component in GRB 190114C.

$t_{\text{start}} \sim t_{\text{stop}}$	S	Cutoff Power-Law Fitting				Band Fitting					Difference		
		K	α	E_c	F	K	α	β	E_p	F	ΔDIC	$p_{\text{DIC,CPL}}$	$p_{\text{DIC,Band}}$
P_1													
-0.067~0.029	8.40	$0.37^{+0.07}_{-0.07} \times 10^{-1}$	$-0.98^{+0.17}_{-0.17}$	891^{+616}_{-519}	$4.68^{+4.85}_{-2.45} \times 10^{-6}$	$0.37^{+0.08}_{-0.08} \times 10^{-1}$	$-0.98^{+0.19}_{-0.19}$	$-6.17^{+2.72}_{-2.71}$	921^{+614}_{-501}	$4.42^{+4.94}_{-1.99} \times 10^{-6}$	0.0	0.5	0.3
0.029~0.141	21.45	$134.00^{+38.90}_{-38.90} \times 10^{-1}$	$-1.11^{+0.08}_{-0.08}$	1170^{+517}_{-479}	$10.37^{+10.65}_{-4.94} \times 10^{-6}$	$0.71^{+0.05}_{-0.05} \times 10^{-1}$	$-1.15^{+0.06}_{-0.07}$	$-5.12^{+2.74}_{-3.12}$	1211^{+386}_{-370}	$12.53^{+3.27}_{-3.19} \times 10^{-6}$	81.7	0.6	1.4
0.141~0.294	39.83	$1.41^{+0.08}_{-0.08} \times 10^{-1}$	$-1.11^{+0.05}_{-0.05}$	944^{+230}_{-232}	$16.99^{+5.07}_{-3.33} \times 10^{-6}$	$1.41^{+0.08}_{-0.08} \times 10^{-1}$	$-1.11^{+0.05}_{-0.05}$	$-6.34^{+2.50}_{-2.54}$	824^{+165}_{-165}	$17.33^{+3.78}_{-2.84} \times 10^{-6}$	0.3	2.6	2.8
0.294~0.415	50.05	$2.78^{+0.17}_{-0.17} \times 10^{-1}$	$-0.90^{+0.05}_{-0.05}$	451^{+65}_{-66}	$21.90^{+4.86}_{-3.63} \times 10^{-6}$	$2.78^{+0.18}_{-0.18} \times 10^{-1}$	$-0.90^{+0.05}_{-0.05}$	$-5.92^{+2.68}_{-2.72}$	492^{+55}_{-56}	$22.58^{+3.64}_{-3.11} \times 10^{-6}$	0.0	2.8	2.9
0.415~0.546	73.35	$4.42^{+0.18}_{-0.18} \times 10^{-1}$	$-0.78^{+0.04}_{-0.04}$	452^{+42}_{-42}	$40.15^{+5.55}_{-5.07} \times 10^{-6}$	$4.44^{+0.18}_{-0.18} \times 10^{-1}$	$-0.78^{+0.04}_{-0.04}$	$-6.21^{+2.53}_{-2.57}$	545^{+39}_{-40}	$41.10^{+4.81}_{-3.84} \times 10^{-6}$	-0.0	2.9	3.0
0.546~0.701	96.49	$6.47^{+0.22}_{-0.22} \times 10^{-1}$	$-0.66^{+0.03}_{-0.03}$	354^{+23}_{-23}	$49.72^{+5.44}_{-5.02} \times 10^{-6}$	$6.63^{+0.26}_{-0.26} \times 10^{-1}$	$-0.65^{+0.04}_{-0.03}$	$-4.05^{+1.24}_{-1.89}$	454^{+26}_{-25}	$54.13^{+6.04}_{-5.79} \times 10^{-6}$	-6.0	2.9	0.8
0.701~1.579	263.62	$7.71^{+0.08}_{-0.08} \times 10^{-1}$	$-0.68^{+0.01}_{-0.01}$	451^{+10}_{-11}	$80.76^{+3.02}_{-2.94} \times 10^{-6}$	$7.72^{+0.08}_{-0.08} \times 10^{-1}$	$-0.68^{+0.01}_{-0.01}$	$-6.43^{+1.96}_{-2.31}$	594^{+10}_{-10}	$81.07^{+2.16}_{-1.95} \times 10^{-6}$	-1.1	3.0	2.6
1.579~1.713	117.21	$8.32^{+0.16}_{-0.16} \times 10^{-1}$	$-0.47^{+0.02}_{-0.02}$	515^{+22}_{-22}	$147.00^{+12.37}_{-11.77} \times 10^{-6}$	$8.32^{+0.16}_{-0.16} \times 10^{-1}$	$-0.46^{+0.02}_{-0.02}$	$-6.73^{+2.01}_{-2.14}$	788^{+25}_{-25}	$146.90^{+9.38}_{-8.28} \times 10^{-6}$	-0.1	3.0	3.0
1.713~1.805	88.47	$8.93^{+0.34}_{-0.34} \times 10^{-1}$	$-0.56^{+0.04}_{-0.04}$	319^{+21}_{-21}	$67.00^{+8.01}_{-7.87} \times 10^{-6}$	$9.12^{+0.41}_{-0.42} \times 10^{-1}$	$-0.54^{+0.04}_{-0.04}$	$-5.38^{+2.41}_{-2.47}$	447^{+26}_{-27}	$70.25^{+10.60}_{-9.94} \times 10^{-6}$	-1.9	2.9	1.9
1.805~1.933	80.82	$6.01^{+0.33}_{-0.33} \times 10^{-1}$	$-0.84^{+0.04}_{-0.04}$	275^{+26}_{-26}	$28.49^{+3.60}_{-3.22} \times 10^{-6}$	$9.62^{+0.41}_{-0.41} \times 10^{-1}$	$-0.57^{+0.04}_{-0.04}$	$-2.15^{+0.10}_{-0.09}$	199^{+27}_{-27}	$42.18^{+14.55}_{-9.59} \times 10^{-6}$	-20.9	2.9	0.5
1.933~2.137	72.22	$3.10^{+0.16}_{-0.16} \times 10^{-1}$	$-1.01^{+0.04}_{-0.04}$	392^{+46}_{-46}	$18.98^{+2.76}_{-2.28} \times 10^{-6}$	$3.11^{+0.16}_{-0.16} \times 10^{-1}$	$-1.01^{+0.04}_{-0.04}$	$-6.43^{+2.35}_{-2.36}$	381^{+32}_{-32}	$19.17^{+2.09}_{-1.81} \times 10^{-6}$	0.4	2.9	3.1
2.137~2.406	63.87	$2.48^{+0.16}_{-0.16} \times 10^{-1}$	$-1.00^{+0.05}_{-0.04}$	301^{+36}_{-36}	$11.75^{+1.70}_{-1.52} \times 10^{-6}$	$2.49^{+0.17}_{-0.17} \times 10^{-1}$	$-1.00^{+0.05}_{-0.05}$	$-6.41^{+2.39}_{-2.41}$	297^{+25}_{-25}	$11.82^{+1.54}_{-1.24} \times 10^{-6}$	0.5	2.8	3.1
2.406~2.452	37.17	$2.83^{+0.19}_{-0.19} \times 10^{-1}$	$-1.01^{+0.06}_{-0.06}$	1040^{+285}_{-291}	$42.69^{+18.02}_{-10.96} \times 10^{-6}$	$2.90^{+0.21}_{-0.21} \times 10^{-1}$	$-1.00^{+0.07}_{-0.07}$	$-4.30^{+2.00}_{-3.02}$	916^{+225}_{-210}	$45.91^{+15.24}_{-10.74} \times 10^{-6}$	-3.8	2.3	1.0
P_2													
2.452~2.642	152.49	$9.41^{+0.14}_{-0.14} \times 10^{-1}$	$-0.35^{+0.02}_{-0.02}$	464^{+15}_{-15}	$169.90^{+11.71}_{-10.59} \times 10^{-6}$	$9.43^{+0.14}_{-0.14} \times 10^{-1}$	$-0.35^{+0.02}_{-0.02}$	$-6.95^{+1.98}_{-2.08}$	763^{+17}_{-18}	$170.30^{+8.70}_{-6.99} \times 10^{-6}$	-0.2	3.0	2.9
2.642~2.882	135.79	$6.40^{+0.10}_{-0.10} \times 10^{-1}$	$-0.51^{+0.02}_{-0.02}$	559^{+22}_{-22}	$117.20^{+8.53}_{-7.44} \times 10^{-6}$	$6.41^{+0.10}_{-0.10} \times 10^{-1}$	$-0.51^{+0.02}_{-0.02}$	$-5.55^{+1.68}_{-2.30}$	827^{+24}_{-23}	$118.90^{+6.59}_{-5.62} \times 10^{-6}$	-2.4	3.0	2.4
2.882~3.088	102.21	$4.47^{+0.09}_{-0.09} \times 10^{-1}$	$-0.53^{+0.02}_{-0.02}$	666^{+33}_{-33}	$102.80^{+8.27}_{-7.82} \times 10^{-6}$	$4.47^{+0.09}_{-0.09} \times 10^{-1}$	$-0.53^{+0.02}_{-0.02}$	$-5.93^{+1.99}_{-2.47}$	974^{+37}_{-37}	$103.50^{+9.94}_{-9.37} \times 10^{-6}$	-1.2	3.0	2.5
3.088~3.208	92.58	$4.99^{+0.11}_{-0.11} \times 10^{-1}$	$-0.45^{+0.03}_{-0.03}$	814^{+50}_{-50}	$180.70^{+22.92}_{-18.31} \times 10^{-6}$	$5.16^{+0.12}_{-0.12} \times 10^{-1}$	$-0.39^{+0.03}_{-0.03}$	$-2.85^{+0.13}_{-0.13}$	1099^{+49}_{-49}	$192.00^{+16.16}_{-15.55} \times 10^{-6}$	-53.8	3.0	4.0
3.208~3.605	147.68	$4.58^{+0.06}_{-0.06} \times 10^{-1}$	$-0.35^{+0.02}_{-0.02}$	619^{+20}_{-20}	$131.60^{+10.15}_{-8.08} \times 10^{-6}$	$4.64^{+0.06}_{-0.07} \times 10^{-1}$	$-0.33^{+0.02}_{-0.02}$	$-2.88^{+0.09}_{-0.24}$	968^{+24}_{-24}	$149.00^{+7.72}_{-7.26} \times 10^{-6}$	-93.1	3.0	4.0
3.605~3.739	80.43	$4.00^{+0.10}_{-0.10} \times 10^{-1}$	$-0.32^{+0.04}_{-0.04}$	594^{+36}_{-36}	$115.80^{+15.62}_{-14.13} \times 10^{-6}$	$4.04^{+0.10}_{-0.10} \times 10^{-1}$	$-0.30^{+0.04}_{-0.04}$	$-3.06^{+0.21}_{-0.20}$	966^{+42}_{-42}	$129.30^{+12.41}_{-11.48} \times 10^{-6}$	-19.7	2.9	3.9
3.739~3.959	140.01	$6.34^{+0.10}_{-0.10} \times 10^{-1}$	$-0.20^{+0.02}_{-0.02}$	533^{+19}_{-19}	$193.50^{+15.29}_{-14.73} \times 10^{-6}$	$6.55^{+0.11}_{-0.11} \times 10^{-1}$	$-0.14^{+0.03}_{-0.02}$	$-2.71^{+0.07}_{-0.07}$	873^{+23}_{-23}	$224.70^{+13.46}_{-13.54} \times 10^{-6}$	-170.4	3.0	4.0
3.959~4.096	129.78	$9.68^{+0.18}_{-0.18} \times 10^{-1}$	$-0.10^{+0.03}_{-0.03}$	399^{+14}_{-14}	$175.70^{+14.96}_{-12.87} \times 10^{-6}$	$9.75^{+0.19}_{-0.19} \times 10^{-1}$	$-0.10^{+0.03}_{-0.03}$	$-3.65^{+0.35}_{-0.23}$	709^{+19}_{-19}	$187.10^{+12.17}_{-10.94} \times 10^{-6}$	-11.0	3.0	3.8
4.096~4.442	171.47	$8.48^{+0.13}_{-0.13} \times 10^{-1}$	$-0.44^{+0.02}_{-0.02}$	365^{+11}_{-11}	$90.91^{+4.75}_{-5.11} \times 10^{-6}$	$8.55^{+0.15}_{-0.15} \times 10^{-1}$	$-0.44^{+0.02}_{-0.02}$	$-3.60^{+0.39}_{-0.21}$	566^{+13}_{-13}	$97.41^{+4.96}_{-4.85} \times 10^{-6}$	-9.2	3.0	3.5
4.442~4.509	67.63	$7.06^{+0.35}_{-0.34} \times 10^{-1}$	$-0.73^{+0.04}_{-0.04}$	350^{+32}_{-33}	$49.84^{+7.13}_{-6.25} \times 10^{-6}$	$7.07^{+0.35}_{-0.36} \times 10^{-1}$	$-0.73^{+0.05}_{-0.05}$	$-5.87^{+2.69}_{-2.78}$	440^{+30}_{-30}	$51.28^{+6.70}_{-5.57} \times 10^{-6}$	-0.4	2.9	2.8
4.509~4.770	142.78	$7.16^{+0.12}_{-0.12} \times 10^{-1}$	$-0.65^{+0.02}_{-0.02}$	493^{+20}_{-20}	$88.02^{+5.56}_{-5.44} \times 10^{-6}$	$7.16^{+0.12}_{-0.12} \times 10^{-1}$	$-0.65^{+0.02}_{-0.02}$	$-6.78^{+2.03}_{-2.13}$	666^{+19}_{-19}	$88.41^{+4.12}_{-3.75} \times 10^{-6}$	0.0	3.0	3.1
4.770~4.950	134.52	$9.70^{+0.21}_{-0.21} \times 10^{-1}$	$-0.45^{+0.02}_{-0.02}$	351^{+14}_{-14}	$96.19^{+6.57}_{-6.45} \times 10^{-6}$	$9.70^{+0.20}_{-0.20} \times 10^{-1}$	$-0.45^{+0.02}_{-0.02}$	$-7.33^{+1.86}_{-1.84}$	542^{+14}_{-14}	$96.30^{+4.52}_{-4.29} \times 10^{-6}$	0.6	3.0	3.2
4.950~5.451	184.67	$6.94^{+0.10}_{-0.10} \times 10^{-1}$	$-0.62^{+0.02}_{-0.02}$	422^{+13}_{-13}	$72.22^{+3.57}_{-3.51} \times 10^{-6}$	$6.94^{+0.10}_{-0.10} \times 10^{-1}$	$-0.62^{+0.01}_{-0.01}$	$-6.97^{+1.97}_{-2.05}$	582^{+13}_{-12}	$72.22^{+2.46}_{-2.36} \times 10^{-6}$	0.1	3.0	3.1
5.451~5.514	77.55	$10.10^{+0.41}_{-0.41} \times 10^{-1}$	$-0.42^{+0.04}_{-0.04}$	302^{+20}_{-20}	$83.08^{+10.90}_{-9.34} \times 10^{-6}$	$10.12^{+0.40}_{-0.40} \times 10^{-1}$	$-0.41^{+0.04}_{-0.04}$	$-6.81^{+2.16}_{-2.15}$	475^{+21}_{-21}	$83.12^{+6.69}_{-6.74} \times 10^{-6}$	0.5	2.9	3.2
5.514~5.689	109.97	$10.10^{+0.43}_{-0.43} \times 10^{-1}$	$-0.55^{+0.03}_{-0.03}$	193^{+10}_{-10}	$37.07^{+3.57}_{-3.20} \times 10^{-6}$	$10.49^{+0.58}_{-0.57} \times 10^{-1}$	$-0.53^{+0.04}_{-0.04}$	$-4.13^{+1.15}_{-1.47}$	270^{+12}_{-12}	$39.58^{+4.22}_{-4.22} \times 10^{-6}$	-5.6	2.9	1.1
5.689~5.808	69.83	$6.33^{+0.59}_{-0.59} \times 10^{-1}$	$-0.89^{+0.06}_{-0.06}$	171^{+20}_{-20}	$17.29^{+3.08}_{-2.54} \times 10^{-6}$	$5.15^{+0.21}_{-0.21} \times 10^{-1}$	$-1.00^{+0.04}_{-0.04}$	$-5.10^{+2.35}_{-3.08}$	226^{+5}_{-5}	$19.52^{+2.96}_{-1.50} \times 10^{-6}$	2.1	2.6	0.9
5.808~6.000	60.35	$2.46^{+0.32}_{-0.32} \times 10^{-1}$	$-1.35^{+0.07}_{-0.08}$	202^{+41}_{-41}	$8.22^{+1.64}_{-1.45} \times 10^{-6}$	$4.53^{+1.21}_{-1.15} \times 10^{-1}$	$-1.06^{+0.13}_{-0.13}$	$-2.20^{+0.11}_{-0.11}$	83^{+11}_{-11}	$11.53^{+5.05}_{-3.72} \times 10^{-6}$	-18.9	1.6	-0.6
6.000~6.436	62.10	$1.02^{+0.10}_{-0.10} \times 10^{-1}$	$-1.63^{+0.06}_{-0.06}$	440^{+133}_{-138}	$5.80^{+1.17}_{-1.17} \times 10^{-6}$	$1.09^{+0.14}_{-0.14} \times 10^{-1}$	$-1.60^{+0.07}_{-0.07}$	$-5.13^{+2.87}_{-3.31}$	139^{+29}_{-29}	$5.98^{+2.08}_{-1.32} \times 10^{-6}$	-2.0	1.0	0.1
6.436~6.867	50.89	$0.71^{+0.07}_{-0.07} \times 10^{-1}$	$-1.73^{+0.05}_{-0.05}$	537^{+201}_{-182}	$4.66^{+0.85}_{-0.66} \times 10^{-6}$	$0.88^{+0.14}_{-0.14} \times 10^{-1}$	$-1.64^{+0.10}_{-0.11}$	$-3.58^{+1.50}_{-2.81}$	113^{+33}_{-40}	$5.21^{+2.31}_{-1.58} \times 10^{-6}$	-19.6	1.4	-15.2
6.867~8.221	64.64	$0.44^{+0.01}_{-0.01} \times 10^{-1}$	$-1.77^{+0.02}_{-0.02}$	892^{+84}_{-86}	$3.55^{+0.14}_{-0.15} \times 10^{-6}$	$0.43^{+0.02}_{-0.02} \times 10^{-1}$	$-1.81^{+0.05}_{-0.05}$	$-4.96^{+2.68}_{-2.72}$	630^{+275}_{-264}	$4.75^{+0.43}_{-0.81} \times 10^{-6}$	-31.8	2.2	-23.1
8.221~9.567	49.76	$0.32^{+0.01}_{-0.01} \times 10^{-1}$	$-1.78^{+0.03}_{-0.03}$	706^{+132}_{-140}	$2.59^{+0.14}_{-0.17} \times 10^{-6}$	$0.29^{+0.01}_{-0.01} \times 10^{-1}$	$-1.85^{+0.03}_{-0.03}$	$-5.02^{+2.64}_{-2.64}$	647^{+264}_{-275}	$3.50^{+0.22}_{-0.37} \times 10^{-6}$	-6.2	2.2	1.5
9.567~12.400	54.86	$0.22^{+0.01}_{-0.01} \times 10^{-1}$	$-1.86^{+0.03}_{-0.03}$	830^{+193}_{-192}	$1.83^{+0.17}_{-0.16} \times 10^{-6}$	$0.21^{+0.02}_{-0.02} \times 10^{-1}$	$-1.91^{+0.06}_{-0.06}$	$-5.15^{+2.52}_{-2.54}$	305^{+362}_{-221}	$2.33^{+0.43}_{-0.52} \times 10^{-6}$	-7.6	2.1	-6.5
12.400~15.547	47.53	$0.17^{+0.01}_{-0.01} \times 10^{-1}$	$-1.93^{+0.03}_{-0.03}$	699^{+207}_{-205}	$1.47^{+0.14}_{-0.14} \times 10^{-6}$	$0.15^{+0.00}_{-0.00} \times 10^{-1}$	$-1.99^{+0.01}_{-0.01}$	$-5.54^{+2.37}_{-2.31}$	512^{+321}_{-312}	$2.11^{+0.06}_{-0.09} \times 10^{-6}$	0.3	2.0	1.0
P_3													
15.547~15.872	38.28	$0.74^{+0.07}_{-0.07} \times 10^{-1}$	$-1.49^{+0.06}_{-0.06}$	552^{+199}_{-182}	$4.59^{+1.03}_{-0.93} \times 10^{-6}$	$0.76^{+0.09}_{-0.10} \times 10^{-1}$	$-1.47^{+0.08}_{-0.08}$	$-5.07^{+2.60}_{-2.62}$	278^{+76}_{-90}	$4.77^{+1.65}_{-0.98} \times 10^{-6}$	-1.8	1.7	0.0
15.872~16.173	49.52	$1.06^{+0.09}_{-0.09} \times 10^{-1}$	$-1.49^{+0.05}_{-0.06}</$										

Figures

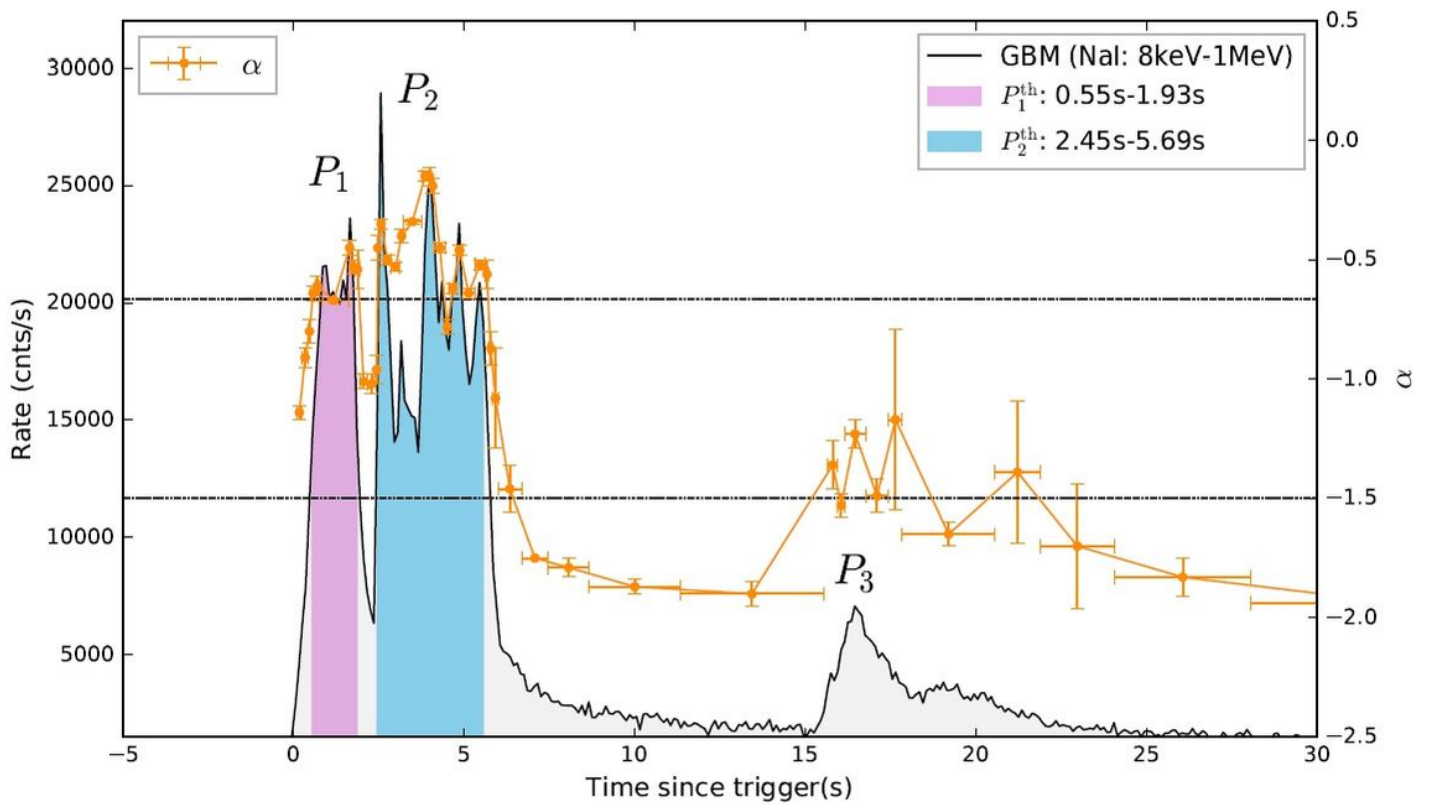


Figure 1

Count lightcurve of Fermi-GBM during the time span of 0- 30 s. Two shaded regions marked with different colors denote the two independent thermally-subdominated episodes: Pth1 (pink) and Pth2 (blue). Two horizontal dashed lines represent the limiting values of $a=-2/3$ and $a=-3/2$ for electrons in the synchrotron slow- and fast-cooling regimes, respectively. The data points connected by solid lines (orange) represent the temporal evolution of the low-energy photon index a of the CPL-only model.

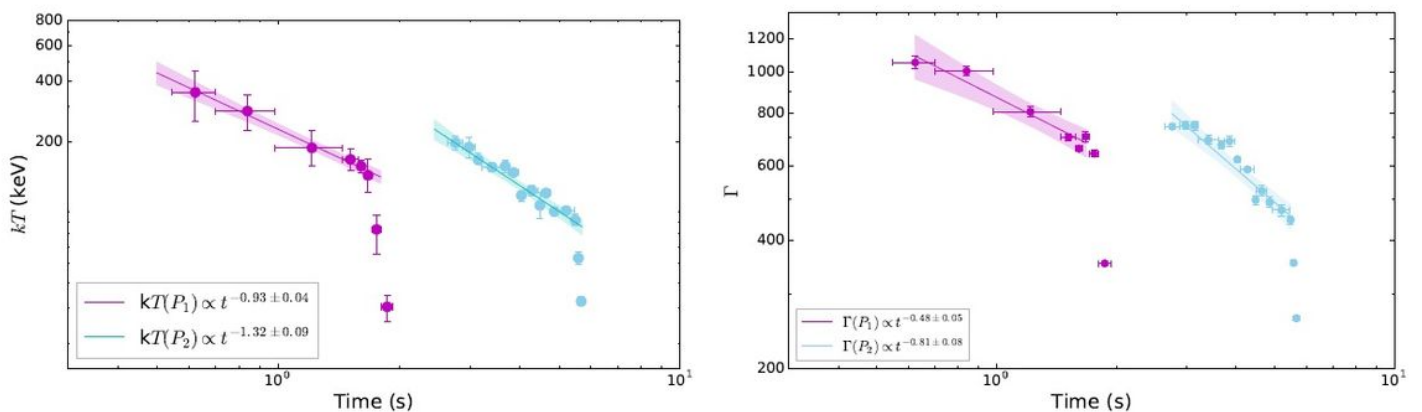


Figure 2

Temporal evolution of the temperature kT (left panel), and bulk Lorentz factor Γ (right panel). The data points indicated by pink and blue colors represent the two different pulses. Solid lines are the best power-law fits to the data for P1 and P1 excluding several points during the drop, and shaded areas are their 2- σ (95% confidence interval) regions. The derived time-resolved evolution of Γ is based on the photosphere properties under the framework of the traditional method²².

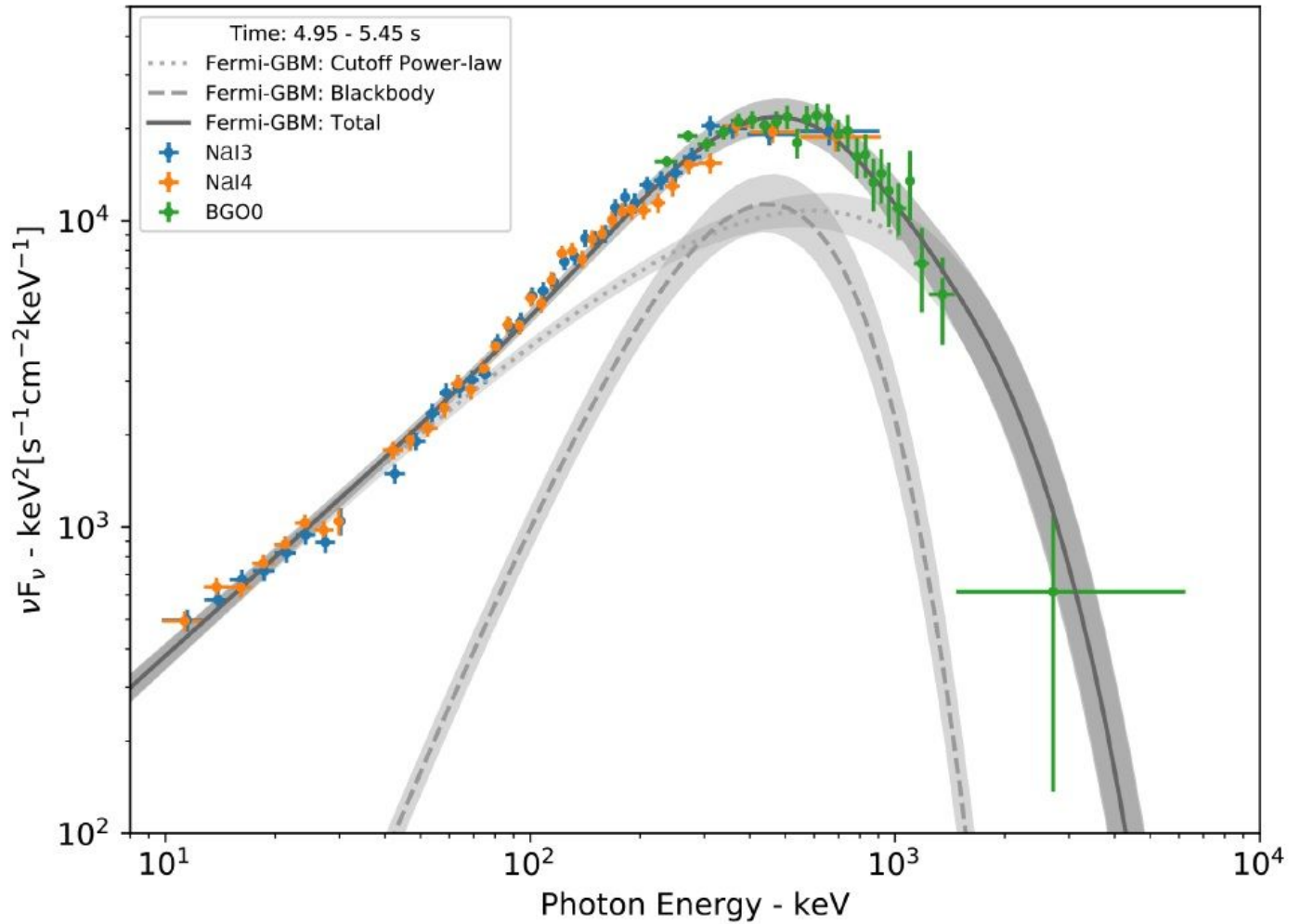


Figure 3

Spectrum from 4:95 s to 5:45 s. The spectrum includes data from Fermi-GBM (2 NaI and 1 BGO detector). The fitting is presented by a solid line, including the components of a Plank blackbody function by a dashed line and a cutoff power-law by a dotted line.